

# **Developing the tracking algorithm for Geant4 based simulated muon data, a step towards muography studies**

*A thesis Submitted  
in Partial Fulfilment of the Requirements  
for the Degree of*  
**MASTER OF SCIENCE**

*by*  
**Abhishek**

HBNI Enrollment No. PHYS11201913003



*to the*  
**School of Physical Sciences**  
**National Institute of Science Education and Research**  
at Bhimpur, Padanpur, P.O. Jatani,  
Khurda – 752050, Odisha, India

**May 16, 2024**

## **DECLARATION**

I hereby declare that I am the sole author of this thesis in partial fulfillment of the requirements for a postgraduate degree from National Institute of Science Education and Research (NISER). I authorize NISER to lend this thesis to other institutions or individuals for the purpose of scholarly research.

Signature of the Student

Date:

The thesis work reported in the thesis entitled "*Developing the tracking algorithm for Geant4 based simulated muon data, a step towards muography studies*" was carried out under my supervision in the School of Physical Sciences at NISER, Bhubaneswar, India.

Signature of the thesis supervisor

School: School of Physical Sciences

Date: May 16, 2024

Signature of the thesis co-supervisor

School:

Date:

## ACKNOWLEDGEMENTS

Acknowledging the invaluable support I have received from various individuals is crucial for the completion of this work.

First and foremost, I extend my heartfelt gratitude to my master's thesis supervisor **Prof. Bedangadas Mohanty** for not only offering me this opportunity but also providing continuous guidance to accomplish the thesis successfully. His unwavering passion for physics has been a constant motivation for me.

I am deeply thankful to my co-guide **Dr. Raveendrababu Karnam** for his consistent support and assistance throughout the project. Additionally, I express my gratitude to **Dr. Varchasvi Kashyap** for his valuable advice and insightful discussions.

I cannot overlook the invaluable contributions of **Dr. Andrea Giammanco** and all the members of the Muography team at the Center for Cosmology, Particle Physics, and Phenomenology (CP3) at UCLouvain for their guidance and support. Special thanks go to Dr. Marwa Al Moussawi for her assistance with the GEANT4 simulation and to Mr. Maxime Lagrange for his help with the image reconstruction algorithm. I am also grateful to Mr. Samip Basnet for introducing me to Muography.

During the experimental phase, I would like to express my appreciation to the scientific assistants at CMRP, namely, Mr. Debasis Barik and Mr. Deepak Kumar, for their assistance in developing the Resistive Plate Chamber and Readout Panel. Lastly, I want to thank my parents, who have always supported and believed in me in every situation. I also want to thank my labmates and friends for their encouragement and support throughout this journey.

## ABSTRACT

This report presents the GEANT4 simulation studies of exploiting the cosmic-ray muons to image special nuclear materials like Uranium and the construction and characterization of the glass Resistive Plate Chambers (RPC) for the portable muon imaging telescope, which will be used for societal applications.

For imaging purposes, the Point of Closest Approach (POCA) algorithm is used to reconstruct the image of a Lead block. The medium and high Z (Z = atomic number) materials can be distinguished and identified using the muon scattering angle distributions. Later, the image reconstruction is improved using the Binned Clustering Algorithm (BCA) to reconstruct the edges of the target and image different Z materials simultaneously.

Two Resistive Plate Chambers (RPCs) of size  $200 \times 200 \times 2 \text{ mm}^3$  are constructed for the muon telescope and two Printed Circuit Board (PCB) based read-out panels are developed. A comprehensive characterization studies are conducted on this RPC, including the measurement of efficiency, charge collection, and time resolution for various gas compositions.

# Contents

<b>1</b>	<b>Cosmic ray muons</b>	<b>1</b>
1.1	Muon interaction with matter . . . . .	2
1.2	Energy loss of muons . . . . .	3
1.3	Muon multiple scattering . . . . .	5
1.4	Atmospheric muons production . . . . .	7
1.5	Time dilation for Cosmic-Ray muons . . . . .	8
<b>2</b>	<b>Muography</b>	<b>12</b>
2.1	History . . . . .	12
2.2	Imaging with cosmic ray muons . . . . .	12
2.3	Muon Scattering Tomography . . . . .	13
2.3.1	Identification of material using MST . . . . .	14
2.3.2	Imaging with MST: Point of Closest Approach (PoCA) . . . . .	15
2.4	Point of Closet Approach . . . . .	15
<b>3</b>	<b>Simulations</b>	<b>18</b>
3.1	Simulation of cosmic ray muons . . . . .	18
3.1.1	Zenith angle distribution of cosmic ray muons simulated using ECoMuG . . . . .	20
3.1.2	Energy distribution of cosmic ray muons simulated using ECoMuG . . . . .	20
3.1.3	Charge distribution of cosmic ray muons simulated using ECoMuG . . . . .	21

3.2	Simulation setup . . . . .	22
3.2.1	Muoscope geometry . . . . .	23
3.3	Analysis pipeline . . . . .	25
3.4	Optimizing of the Muoscope geometry . . . . .	25
3.4.1	Acceptance of the muon telescope . . . . .	29
3.4.2	Differentiating High-Z material using Muon Tomography . . . . .	30
3.5	Imaging: Point of Closest Approach (PoCA) . . . . .	32
3.5.1	Scattering angle cut . . . . .	33
3.5.2	Voxelization of the 3D space . . . . .	34
3.6	Binned Clustering Algorithm (BCA) . . . . .	35
3.6.1	Parametrizing the accuracy of the BCA algorithm . . . . .	36
3.6.2	Input Parameters for BCA algorithm . . . . .	39
3.7	Imaging Spent Nuclear Fuel Dry Cask with BCA . . . . .	39
<b>4</b>	<b>Construction and characterization of Resistive Plate Chamber</b>	<b>43</b>
4.1	Resistive Plate Chamber (RPC) . . . . .	43
4.2	Building the RPC and signal read-out panel . . . . .	45
4.3	RPC gas mixture . . . . .	47
4.4	Current-Voltage (I-V) characteristics of glass RPC . . . . .	48
4.5	Muon Telescope: Trigger Criteria . . . . .	49
4.6	RPC Efficiency Studies . . . . .	52
4.6.1	RPC signal . . . . .	52
4.6.2	RPC efficiency . . . . .	54
4.7	Charge collection . . . . .	55
4.8	Time resolution of RPC . . . . .	57
4.9	Relative humidity test on acrylic chamber . . . . .	59

---

**CONTENTS**

4.10 Summary and future prospects . . . . .	62
4.10.1 Future prospects . . . . .	62
<b>Appendix A</b>	<b>64</b>
4.1 RPC: Avalanche and Streamer . . . . .	64
4.1.1 Avalanche Mode . . . . .	64
4.1.2 Streamer Mode . . . . .	65
4.2 Scattering angle distribution of Iron . . . . .	66
4.3 Scattering angle distribution of Uranium . . . . .	66

# List of Figures

1.1	Stopping power . . . . .	2
1.2	Nuclei flux of primary cosmic rays . . . . .	8
1.3	Cosmic ray muons vertical flux . . . . .	11
2.2	Muon radiography and tomography . . . . .	13
2.3	Muon scatters multiple times in a target. . . . .	14
2.4	Two tracks $P_1 P_2$ and $P_3 P_4$ in 3D space. $P_a P_b$ is the shortest distance between two tracks. The Midpoint of $P_a P_b$ is denoted a $P_o$ , which is the Point of Closet Approach (PoCA) point. . . . .	16
3.1	Cosmic Ray Muon zenith angle distribution generated using ECoMuG. . . . .	20
3.2	Cosmic Ray Muon energy distribution generated using ECoMuG. . . . .	21
3.3	Cosmic Ray Muon charge distribution generated using ECoMuG. . . . .	21
3.4	Cosmic Ray Muon azimuth angle distribution generated using ECoMuG. . . . .	22
3.5	Muon telescope simulated with GEANT4. . . . .	24
3.6	Simulated muon tracks across the muon telescope. . . . .	24
3.7	Illustration for determining the spatial resolution. . . . .	26
3.8	Illustration for determining the scattering angles distribution. . . . .	27
3.9	The residuals, resulting in a Gaussian distribution with a standard deviation of 8.41 mm. . . . .	28
3.10	The spatial resolution as a function of the distance between the Do-D1 and D2-D3. . . . .	28
3.11	Schematic to show the calculation of angular resolution . . . . .	29
3.12	Acceptance of the muon telescope on the red axis and inverse of the angular resolution on the blue axis. . . . .	30
3.13	Scattering angle distribution without any target. The standard deviation is 4.2 mrad. . . . .	31
3.14	The scattering angle distribution for the lead block of $100 \times 100 \times 100$ mm <sup>3</sup> size. The obtained standard deviation is 12.34 mrad, which is close to the theoretically calculated value as shown in Table 3.4. . . . .	31
3.15	Without Acrylic boxes . . . . .	34
3.16	With Acrylic boxes . . . . .	34
3.17	Demonstration of voxelization and BCA. . . . .	35
3.18	Reference histogram of a 100 mm <sup>3</sup> Lead block. . . . .	37
3.19	2D image of $100 \times 100 \times 100$ mm <sup>3</sup> Lead block reconstructed with POCA algorithm (Error = 0.122). . . . .	38
3.20	2D image of $100 \times 100 \times 100$ mm <sup>3</sup> Lead block reconstructed with Binned Clustering Algorithm (Error = 0.002). . . . .	38
3.21	A dry Cask is placed in between detectors. . . . .	40
3.22	Shows a 2D image, an XZ projection, reconstructed using BCA. The presence of Uranium rods is visible in the center of the cask. . . . .	40

---

LIST OF FIGURES

3.23	A dry cask made of concrete and steel containing Uranium (SNF) and copper rods is simulated in GEANT4. . . . .	41
3.24	Presents the XY projection using the BCA reconstruction. . . . .	41
4.1	RPC schematic . . . . .	44
4.2	Avalanche formation inside the gas gap . . . . .	44
4.3	Surface resistance of graphite coated glass electrode (a) G5 and (b) G6. . . . .	45
4.4	(a) A $200 \times 200 \text{ mm}^2$ glass RPC (b) A Printed Circuit Board (PCB) panel is used to develop 16 strips of copper read-out for reading the RPC signal. . . . .	46
4.5	IV Characteristics of a glass RPC. . . . .	49
4.6	The muon telescope schematic comprises plastic scintillators, with Scintillators 1 and 3 of dimensions $400 \times 200 \times 10 \text{ mm}^3$ , while Scintillator 2 dimensions $300 \times 40 \times 10 \text{ mm}^3$ . . . . .	50
4.7	A muon telescope is used for measuring the efficiency of the glass RPC. . . . .	50
4.8	A $200 \times 200 \text{ mm}^2$ glass RPC. . . . .	51
4.9	CAEN SY4527 power supply system is used for providing high voltage to the RPC. . . . .	51
4.10	A RPC and trigger signal recorded by the oscilloscope. . . . .	52
4.11	The threshold for the RPC pulse is set at $5\sigma$ of the baseline noise. . . . .	53
4.12	RPC efficiency plot. . . . .	55
4.13	Charge spectra at 10.0 kV. . . . .	56
4.14	Charge spectra at 10.2 kV. . . . .	56
4.15	Charge spectra at 10.4 kV. . . . .	57
4.16	Time resolution of RPC. . . . .	58
4.17	Acrylic chamber for housing the RPC. . . . .	60
4.18	Humidity levels are monitored both outside and inside the acrylic chamber for 32 days. Red points represent humidity levels inside the chamber, while black points represent humidity levels inside the chamber. . . . .	61
4.19	Temperature is monitored both outside and inside the acrylic chamber for 32 days. Red points represent temperature inside the chamber, while black points represent the temperature inside the chamber. . . . .	61
4.1	(a) Scattering angle distribution in XZ plane. (b) Scattering angle distribution in YZ plane. . . . .	66
4.2	Uranium block of size $100 \times 100 \times 100 \text{ mm}^3$ is used as target. (a) Scattering angle distribution in XZ plane. (b) Scattering angle distribution in YZ plane. . . . .	66

# List of Tables

3.1	Input and Output Parameters of Ecomug Generator. . . . .	19
3.2	Acceptance and angular resolution of muon telescope as a function of the distance between the D <sub>1</sub> and D <sub>2</sub> as shown in Figure 3.5. . . . .	29
3.3	Properties of selected elements . . . . .	31
3.4	Comparison of theoretically calculated using Equation 1.6 and sim- ulated sigma values for different materials of thickness 100 mm. . . . .	32
3.5	Descripton dry cask geometry . . . . .	42
4.1	Flush rate of gases in Standard Cubic Centimeters per Minute (SCCM). . . . .	54
4.2	Efficiency and charge collection of RPC as a function of SF <sub>6</sub> concen- tration. . . . .	58
4.3	SF <sub>6</sub> concentration and time resolution. . . . .	59

# Chapter 1

## Cosmic ray muons

In 1936, Carl D. Anderson and Seth Neddermeyer observed particles in cosmic radiation that exhibited different curling patterns<sup>1</sup> in the cloud chamber than other known particles when passing through magnetic fields [1]. Initially, these particles were assumed to have greater mass than electrons but smaller than protons. They were once thought to be the particles hypothesized by Hideki Yukawa, a Japanese scientist, 1935 to explain the strong force binding protons and neutrons in atomic nuclei due to their mass [2]. However, it was later discovered that muons belong to the lepton group, as they never interact with nuclei or other particles through the strong force. Muons are unstable elementary particles; the mass of muon is  $\approx 105.6$  MeV [3] 200 times heavier than electrons, with a lifetime of  $\approx 2.2 \mu\text{s}$  [3]. It decays into an electron and two types of neutrinos via the weak interaction.

$$\mu^- \rightarrow e^- + \bar{\nu}_e + \nu_\mu \quad (1.1)$$

$$\mu^+ \rightarrow e^+ + \nu_e + \bar{\nu}_\mu \quad (1.2)$$

<sup>1</sup>The muon has the same charge as both the proton and the electron, but its mass differs from both particles. This difference in mass results in a distinct curling pattern in its trajectory.

## 1.1 Muon interaction with matter

Like other fundamental particles, muons lose energy as they traverse through matter. However, unlike other charged particles, muons can travel through hundreds of meters of rock without decaying. Muons exhibit a remarkable ability to penetrate matter deeply. They primarily lose energy through Coulomb scattering with atomic electrons and Bremsstrahlung radiation.

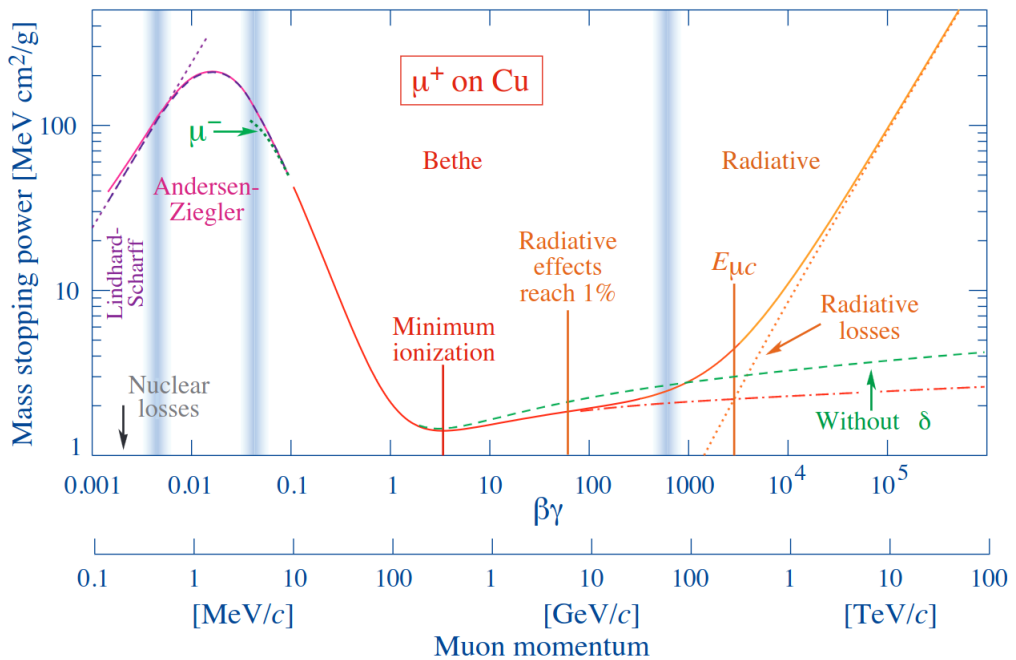


Figure 1.1: The stopping power, denoted as  $\langle -\frac{dE}{dx} \rangle$ , for positive muons in copper is represented as a function of momentum  $p = M\beta c\gamma$ . The solid curves in the figures indicate the total stopping power. Note that within the range of cosmic muon momentum, muons have the lowest ionization rate compared to other charged particles. [4] .

**Ionization** occurs when a muon passes through matter and interacts with electrons inelastically. Because muons are much heavier than electrons, they can knock out electrons from their orbital during collisions, transferring some of their energy to the electrons. This process results in the ionization of atoms. Ionization

is the primary mode of energy loss for muons. Muons also scatter off nuclei, but this interaction is primarily elastic, merely causing the muon to deviate without energy loss.

**Bremsstrahlung radiation:** When muons pass through matter, they can also emit electromagnetic radiation known as Bremsstrahlung. This radiation occurs when the muon is deflected by the electromagnetic field of an atomic nucleus, causing it to emit photons. However, this phenomenon is negligible for cosmic muons since their energies are typically less than 100 GeV, and the rest of the mass is heavier than other particles.

Cosmic muons with energies below 100 GeV are less likely to emit Bremsstrahlung radiation since the loss of energy via Bremsstrahlung radiation is proportional to  $\frac{1}{m_\mu^4}$  where  $m_\mu$  is the mass of muons and which is 200 times heavier than electrons. As a result, Bremsstrahlung radiation does not significantly affect cosmic muons. Cosmic muons (0.1 - 100 GeV) are the least ionizing particles. See Figure 1.1. Therefore, their penetration ability is higher than any other charged particle.

## 1.2 Energy loss of muons

Each collision has a small energy loss, and many collisions in dense material. Thus, one can work with average energy loss  $\langle \frac{dE}{dx} \rangle$ . This is described by the **Bethe-Bloch** formula [5]. However, this formula is applicable only within a certain energy range of the incoming particle. To model the mean energy loss (stopping power) of muons, the following formula can be used [4]:

$$-\frac{dE}{dx} = a(E) + b(E)E \quad (1.3)$$

Where  $a(E)$  represents the stopping power due to ionization energy loss (elec-

tronic processes), and  $b(E)$  represents the stopping power due to radiative processes (Bremsstrahlung, direct production of  $e^+e^-$  pairs, and photonuclear interactions).

For example, a muon with an energy<sup>2</sup> of 4 GeV passes through Aluminium. Given that the ionization energy loss  $a_{Al}$  is approximately 2 MeV/(g/cm<sup>2</sup>) and the radiative energy loss  $b_{Al}$  is approximately  $4.4 \times 10^{-6}$  (g/cm<sup>2</sup>)<sup>-1</sup>, we can calculate the range  $\hat{R}(E)$  as:

$$\hat{R}(E) = \int_0^E \frac{1}{a + bE'} dE' = \frac{-1}{b} \ln \left( 1 + \frac{bE}{a} \right) \Big|_0^{4\text{GeV}} = 1991.25 \text{ g/cm}^2 \quad (1.4)$$

Given the density of Aluminium  $\rho_{Al} = 2.71 \text{ g/cm}^3$  [4], we can then find the actual range  $R(E)$  as  $R(E) = \frac{\hat{R}(E)}{\rho} \approx 734.78 \text{ cm}$ , or approximately 7 m. This calculation underscores the significant penetration capability of muons, making them a valuable tool for probing the interiors of large, dense objects.

Muon is abundant at sea level compared to other charged particles, i.e., electrons, protons, etc. The following reasons make muons the most abundant charged particles at sea level.

1. Muons have a longer lifetime of around 2.2  $\mu\text{s}$ . This characteristic makes them the predominant charged particles at sea level, outlasting other unstable particles.
2. The mass of muons is higher than that of electrons. This makes it traverse kilometers of rock before any interaction, unlike electrons that lose their energy within mere centimeters due to their substantial electromagnetic radiation.
3. Unlike protons and neutrons, muons (leptons) do not have hadronic interactions. This property allows them to pass through longer distances.

---

<sup>2</sup>Average energy of cosmic muons is  $\approx 4 \text{ GeV}$  [6]

4. Muons are classified as Minimum Ionizing Particles (MIPs). This means that their average rate of energy loss through matter is near the minimum. Please see Figure 1.1.

### 1.3 Muon multiple scattering

The previous section discusses muon energy loss through inelastic scattering with electrons. However, muons also interact with atomic nuclei. Because nuclei are much heavier than muons, the muon's trajectory deviates due to the electromagnetic force of the nucleus, a phenomenon known as scattering. The scattering of a charged particle can be described by the Rutherford scattering formula [7].

$$\frac{d\sigma}{d\Omega} = \left( \frac{Z_1 Z_2 e^2}{8\pi\epsilon_0 m v^2} \right)^2 \frac{1}{\sin^4(\theta/2)} \quad (1.5)$$

In Equation 1.5,  $d\sigma/d\Omega$  is the differential cross section,  $Z_1$  and  $Z_2$  are the atomic numbers of the two particles,  $e$  is the elementary charge,  $\epsilon_0$  is the permittivity of free space,  $m$  is the mass of the particle,  $v$  is the velocity of the particle, and  $\theta$  is the scattering angle. However, this formula is valid for very thin layer of matter<sup>3</sup>. In the case of the thick target, there is a possibility of multiple atoms scattering. Depending on the thickness of the material traversed and the average number of scattering processes, we distinguish three possibilities:

1. For very thin objects, the chance of having more than one large scattering process is minimal, and it can be represented as a single Rutherford deflection (single scattering).
2. There are many large scattering processes for thick thicknesses, but the

---

<sup>3</sup>The Rutherford experiment was conducted with a thin layer of gold foil to ensure that only a small number of atoms could interact with alpha particles

overall energy loss is small. In this case, we can statistically determine the probability of a given overall deflection using various approximations. This is called multiple scattering, the most commonly treated condition, even in practical applications.

In muography, the process is statistically treated, considering that the average number of scatterings is high and the energy loss is small.. Molière's theory [8] describes the net scattering distribution as a function of thickness. The central limit theorem states that the total of many distributions, in this case, single Coulomb scatterings, can be approximated by a Gaussian. This Gaussian approximation describes 98% of the actual distribution [3], with a standard deviation  $\sigma(\Delta\theta)$  that is well approximated across a wide range of atomic numbers (Z) and for only thick objects.

$$\sigma(\Delta\theta) = \frac{z \cdot 13.6 \text{ MeV}}{p\beta c} \sqrt{\frac{x}{X_0}} \left[ 1 + 0.038 \cdot \ln \left( \frac{x}{X_0} \right) \right] \quad (1.6)$$

Here,  $p$  and  $\beta c$  are the momentum and velocity of the muon,  $z = 1$  is the charge of the muon, and  $x$  and  $X_0$  are the target's thickness and characteristic radiation length, respectively. The radiation length is the mean distance over which an electron loses all but  $1/e$  of its energy and can be written as follows:

$$X_0 = \left[ \frac{A \cdot 716.4 \text{ g cm}^{-2}}{Z(Z+1) \ln(287/\sqrt{Z})} \right] \left[ \frac{1}{\rho} \right] \quad (1.7)$$

Here,  $\rho, A$  and  $Z$  are the material's density, atomic weight, and atomic number. The approximate  $\rho \cdot Z^2$  dependence for large  $Z$  characterizes the sensitivity to dense objects with a high atomic number. Thus, the muon scattering angle distribution width can be useful in identifying material atomic number (Z).

## 1.4 Atmospheric muons production

All characteristics discussed in the previous section indicate that muons can be effectively utilized to investigate the interior of large and dense objects. **Muography** utilizes cosmic ray muons to investigate the interior of dense or large objects. These muons are produced in the upper atmosphere when cosmic rays originating from outer space collide with the nuclei of the atmosphere gases, mainly oxygen ( $O_2$ ) and nitrogen ( $N_2$ ) molecules. The cosmic rays are high-energy particles, Most of these cosmic rays, about 89% are protons and about 10% helium nuclei and 1% of other heavier elements, such as calcium and iron [9]. Most of these cosmic rays are of galactic origin, like supernovas. The cosmic rays are accelerated by a combination of diffusive shock acceleration (DSA) and diffusive propagation in the Galaxy. This is commonly known as the supernova remnant paradigm [10]. These cosmic ray particles enter the Earth's atmosphere and collide with the upper atmosphere gas molecules. The nature of collision is strong interaction, which results in the formation of new particles like pions ( $\pi^\pm, \pi^0$ ) and kaons ( $K^\pm, K^0, K_0^S, K_0^L$ ). These pions (lifetime= $2.6 \times 10^{-2} \mu s$ ) and kaons (lifetime= $1.2 \times 10^{-2} \mu s$ ) decay into muons as shown in the following Equations (1.8 - 1.11).

$$\pi^+ \rightarrow \mu^+ + \nu_\mu \quad (1.8)$$

$$\pi^- \rightarrow \mu^- + \bar{\nu}_\mu \quad (1.9)$$

$$K^+ \rightarrow \mu^+ + \nu_\mu \quad (1.10)$$

$$K^- \rightarrow \mu^- + \bar{\nu}_\mu \quad (1.11)$$

Most of the muons are produced in the upper atmosphere around 15 km high above sea level. The Equation 1.8 and 1.9 shows the decay of charged pion into

a muon and Equation 1.10 and 1.11 shows the decay of charged kaon into muon respectively [11].

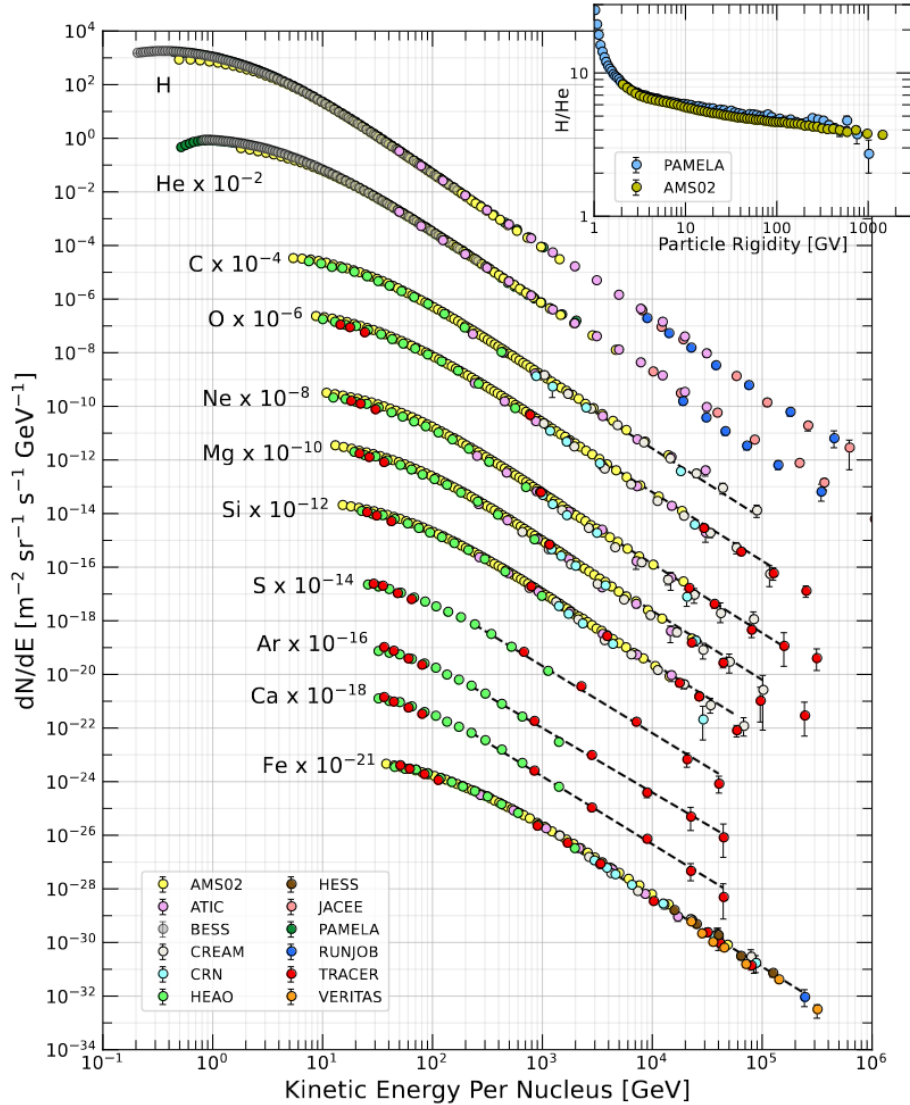


Figure 1.2: Nuclei fluxes of primary cosmic radiation, measured in particles per energy per nucleus, are plotted against energy per nucleus [9].

## 1.5 Time dilation for Cosmic-Ray muons

Pions ( $\pi^+, \pi^0, \pi^-$ ) and Kaons ( $K^+, K_S^0, K_L^0, K^-$ ) are the subnuclear particles most abundantly produced by these cosmic rays collision with air molecules in the upper

atmosphere, and when they are charged, their dominant decay mode : Charged Pions ( $\pi^\pm$ ) predominantly decay into muons ( $\mu^\pm$ ) and muon neutrinos ( $\nu_\mu$  or  $\bar{\nu}_\mu$ ) approximately 99.99% of the time. Similarly, charged kaons ( $K^\pm$ ) decay into muons and muon neutrinos about 64% of the time, with an additional 3% of cases involving the production of a  $\pi^0$  particle. When charged kaons do not directly decay into muons, they mostly decay into two or three pions ( $\pi^\pm\pi^0$ ,  $\pi^\pm\pi^\pm\pi^\mp$ , or  $\pi^\pm\pi^0\pi^0$ ), and these pions, if charged, can further decay into muons.

The short-lived  $K_S^0$  particle almost always decays into pion pairs ( $\pi^+\pi^-$  or  $\pi^0\pi^0$ ). On the other hand, the long-lived  $K_L^0$  particle can decay into triplets ( $\pi^+\pi^-\pi^0$  or  $\pi^0\pi^0\pi^0$ ). Additionally,  $K_L^0$  produces muons in approximately 27% of its decays through the channel  $K_L^0 \rightarrow \pi^\pm\mu^\mp\bar{\nu}_\mu$  ( $\nu_\mu$ ).

These decay processes contribute significantly to the production of muons and other particles in the interactions of cosmic rays with the atmosphere, leading to a diverse range of muon flux observations at the Earth's surface. Muon half-life is 2.2  $\mu$ s and the average distance between the upper atmosphere and the earth's surface is  $\approx$ 14 Km. Hence, one can ask how muons reach in such a short time. When muons are created in the upper atmosphere from interactions of high-energy cosmic rays with atmospheric nuclei, they are typically produced with high velocities close to the speed of light ( $\approx 0.99c$ ). As they move at such relativistic speeds, they experience time dilation, a fundamental concept in Einstein's theory of special relativity. Time dilation means time appears to pass more slowly for an object in motion relative to an observer at rest.

Due to time dilation, muons moving at relativistic speeds experience time at a slower rate than an observer at rest on Earth. This means that from the muon's perspective, its lifetime appears longer. As a result, muons can travel much farther than they would if they were at rest before decaying.

Using relativistic effects, time dilation will be:

$$\Delta t' = \gamma \Delta t \quad (1.12)$$

where  $\Delta t'$  is the dilated time,  $\Delta t$  is the proper time, and  $\gamma$  is the Lorentz factor.

The Lorentz factor is given by:

$$\gamma = \frac{1}{\sqrt{1 - \frac{u^2}{c^2}}} \quad (1.13)$$

Where  $u$  is the relative velocity of cosmic muons, and  $c$  is the speed of light.

Substituting  $u = 0.999c$  [12] into the equation for the Lorentz factor, we get:

$$\gamma = \frac{1}{\sqrt{1 - \left(\frac{0.999c}{c}\right)^2}} \approx 22 \quad (1.14)$$

Given that the Lorentz factor  $\gamma$  is approximately 22 and the proper lifetime  $\Delta t$  is  $2.2 \mu s$ , we can calculate the dilated time  $\Delta t'$  as follows:

$$\Delta t' = \gamma \Delta t = 22 \times 2.2 \times 10^{-6} s = 48.4 \times 10^{-6} s \quad (1.15)$$

The average speed of cosmic muons is  $u \approx 0.999c$  and the time  $\Delta t$  is  $48.4 \mu s$ , we can calculate the range  $d$  as follows:

$$d = u \Delta t' = 0.999c \times 48.4 \times 10^{-6} s \approx 14408 m \quad (1.16)$$

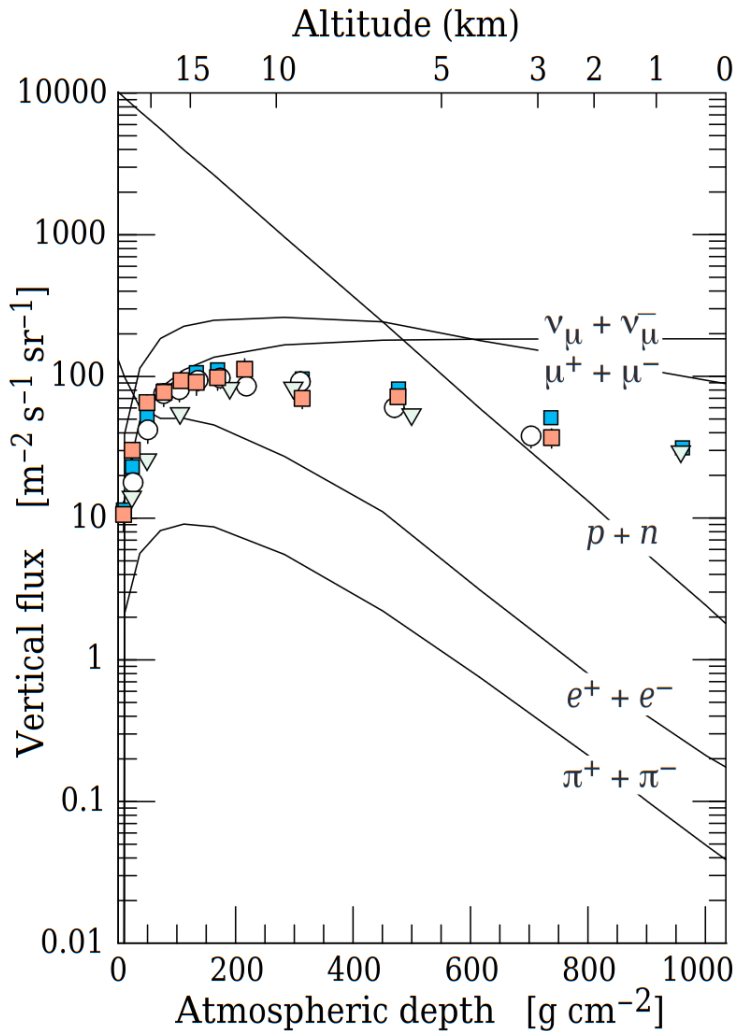


Figure 1.3: Vertical flux of cosmic rays ( $\leq 1$  GeV) in Earth's atmosphere [9].

Without relativistic effects, cosmic muons won't be able to reach Earth's surface. It can travel 660 meters if we don't consider time dilation. However, considering time dilation, it travels  $\approx 14.4$  km. It's fascinating to see that the high flux of cosmic muons observed at the sea surface strongly supports the theory of Special Relativity. This shows how Special Relativity can explain the high flux of cosmic muons at the Earth's surface, while classical mechanics cannot explain it.

# Chapter 2

## Muography

In this chapter, the basic introduction of muography is discussed as its applications and the motivation behind the study of muography. Muography is a non-destructive technique that uses cosmic ray muons to investigate the interior of dense or large objects.

### 2.1 History

In 1955, Eric George used muography [13]. He used it to discover how thick the ice was over a tunnel in Australia. He did this by looking at special particles called cosmic muons that come from the upper atmosphere and can pass through the ice. By comparing the number of muons coming from the open sky and the number after passing through the ice, he calculated the thickness of the ice. In 1969, Luis Alvarez's team used spark chambers and scintillator counters to search for hidden chambers in the Pyramid of Khafre in Egypt [14].

### 2.2 Imaging with cosmic ray muons

Muography can be classified into broad categories:

- **Muon Radiography:** Muon radiography is an imaging method that measures the muon flux before and after passing through a target. This technique relies on the absorption of muon flux by the target [15]. For instance, dense

objects can absorb muons, while regions with voids show lower absorption, indicating the presence of a void within the object. Please see Figure 2.2a.

- **Muon Scattering Tomography (MST):** Muon Scattering Tomography is an imaging method that exploits the cosmic muon scattering inside the target. It requires two detectors before and after the target. Please see Figure 2.2b.

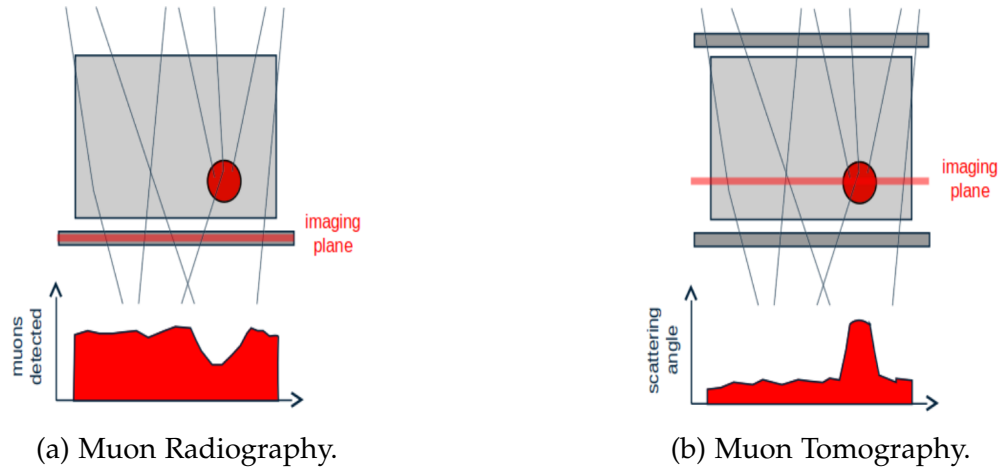


Figure 2.2: (a) Radiography based on the absorption of cosmic muons flux and figure (b) tomography based on scattering of cosmic muons [16].

## 2.3 Muon Scattering Tomography

This thesis primarily focuses on Muon Scattering Tomography (MST). As outlined in the previous section, MST relies on understanding the scattering behavior of cosmic muons. Because muon trajectories exist in three-dimensional space, they can scatter in all three dimensions, thereby revealing the inner structure of the target in three dimensions. This process is referred to as "Tomography". As shown in Figure 2.3 muon scatters multiple times, deviating from its original trajectory (incoming). By measuring the difference between the incoming ( $\theta_{in}$ ) and outgoing ( $\theta_{out}$ ) muon trajectories angles, the scattering angle can be calculated i.e.

$\Delta\theta = \theta_{\text{out}} - \theta_{\text{in}}$ . The scattering angle distribution can be used to infer the material properties of the target. As shown in the Equation 1.6, the  $\Delta\theta$  follows the Moller scattering formula which says that the width (standard deviation  $\sigma(\Delta\theta)$ ) of the scattering angle distribution is directly proportional to the atomic number ( $Z$ ) of the target material.

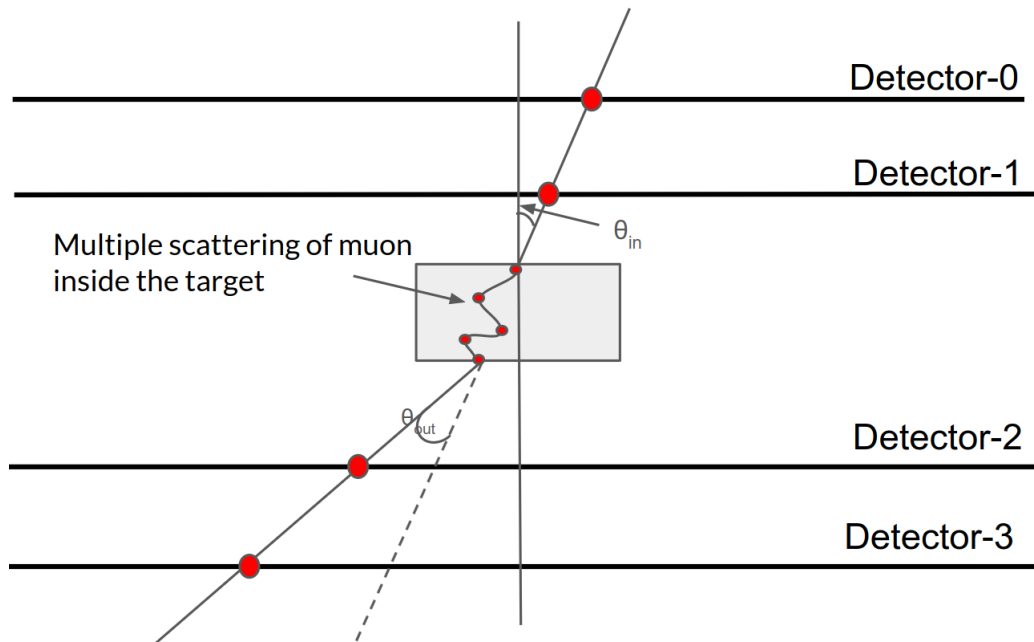


Figure 2.3: Muon scatters multiple times in a target.

### 2.3.1 Identification of material using MST

In Figure 2.3, a target is placed between the upper and lower trackers. Each tracker, both upper and lower, is equipped with two detectors, which are the minimum requirements for MST. The process of reconstructing the scattering angle requires track information (a line). The reconstruction of a track requires at least two points, hence the need for two detectors before the target (for the incoming track) and two after the target (for the outgoing track). This scattering angle distribution can be used for the identification of the material as given in Equation 1.6.

### 2.3.2 Imaging with MST: Point of Closest Approach (PoCA)

MST can be used to image the target by reconstructing the scattering vertices. In principle, there should be more scattering vertices in high Z and dense material as compared to low Z material. The scattering vertices can be reconstructed by finding the point of closest approach (PoCA). In Figure 2.3, it is shown that muon can scatter multiple times. However, it is possible to find a single scattering point that approximately includes the contribution of multiple scattering vertices. PoCA is an algorithm that can be used to find the scattering vertices.

## 2.4 Point of Closet Approach

- The shortest line segment between two lines "a" and "b" can be found by minimizing the distance function  $\|P_b - P_a\|^2$  and solving the resulting equations for  $\mu_a$  and  $\mu_b$ , then substituting these values into the line equations to obtain the intersection points.
- The shortest line segment between two lines is perpendicular to both lines. This line segment can be determined by finding the direction vector of each line and taking their cross-product to get the direction vector of the shortest line. The point of intersection of this shortest line with one of the given lines can then be calculated, giving the coordinates of the nearest point on that line. Please see Figure 2.4.

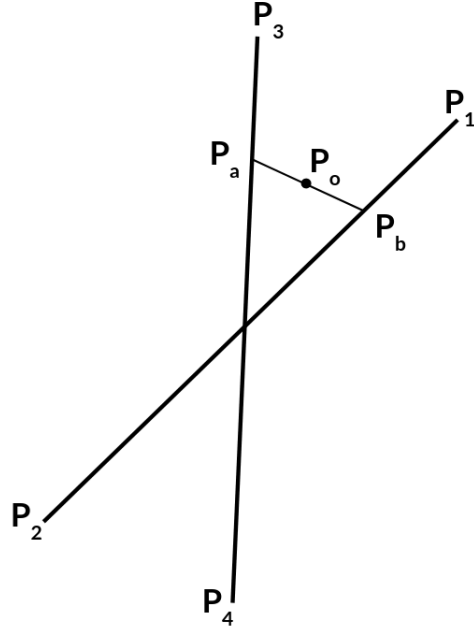


Figure 2.4: Two tracks  $P_1P_2$  and  $P_3P_4$  in 3D space.  $P_aP_b$  is the shortest distance between two tracks. The Midpoint of  $P_aP_b$  is denoted a  $P_o$ , which is the Point of Closet Approach (PoCA) point.

In Figure 2.4, two tracks  $P_1P_2$  and  $P_3P_4$  are shown in 3D space. The midpoint of the shortest line segment between  $(P_aP_b)$  two lines ( $P_1P_2$  and  $P_3P_4$ ) is called the **Point of Closet Approach (PoCA)**. The dot product equations for finding the shortest line segment between two lines are

$$(P_a - P_b) \cdot (P_2 - P_1) = 0$$

$$(P_a - P_b) \cdot (P_4 - P_3) = 0$$

Expanding these equations with the line equations:

$$(P_1 - P_3 + \mu_a(P_2 - P_1) - \mu_b(P_4 - P_3)) \cdot (P_2 - P_1) = 0$$

$$(P_1 - P_3 + \mu_a(P_2 - P_1) - \mu_b(P_4 - P_3)) \cdot (P_4 - P_3) = 0$$

$$(P_1 - P_3) \cdot (P_2 - P_1) + \mu_a(P_2 - P_1) \cdot (P_2 - P_1) - \mu_b(P_4 - P_3) \cdot (P_2 - P_1) = 0$$

$$(P_1 - P_3) \cdot (P_4 - P_3) + \mu_a(P_2 - P_1) \cdot (P_4 - P_3) - \mu_b(P_4 - P_3) \cdot (P_4 - P_3) = 0$$

The equations for finding  $\mu_a$  and  $\mu_b$ , which determine the shortest line segment between two lines, are:

$$\mu_a = (d_{1343} d_{4321} - d_{1321} d_{4343}) / (d_{2121} d_{4343} - d_{4321} d_{4321})$$

$$\mu_b = (d_{1343} + \mu_a * d_{4321}) / d_{4343}$$

where  $d_{mnop} = (x_m - x_n)(x_o - x_p) + (y_m - y_n)(y_o - y_p) + (z_m - z_n)(z_o - z_p)$ .

To compute the Point of Closest Approach (PoCA), the necessary 3D coordinates from all four detector layers must be obtained. This data can be derived from the GEANT4 simulated detector, shown in Figure 3.5.

# Chapter 3

## Simulations

This chapter discusses the simulation of cosmic ray muons and their interaction with matter. The cosmic ray muons are simulated using an external library ECoMuG [17]. It is a parameterized simulation of cosmic ray muons. The muon scattering tomography simulation is performed using the GEANT4 [18] toolkit for simulating particle and matter interaction. Please find all the simulation study codes on my GitHub account at <https://github.com/abhich2507>.

### 3.1 Simulation of cosmic ray muons

There are many muon generators, and we can divide them based on the following criteria:

- **Cosmic-ray air shower (CRAS) generators:** Simulate the complete cascade of secondary particles initiated by primary cosmic rays.
- **Parametric generators:** Utilize a parameterized representation of the cosmic ray muon flux derived either from experimental data or the results of simulations with CRAS generators.
- **Special generators:** Specifically designed for underground, high-altitude, or underwater experiments.

In our study, we employed a parametric generator known as **ECoMuG: An Efficient COsmic MUon Generator** for cosmic-ray muon applications [17]. EcoMug

is a header-only C++11 library that relies on a parametrization of ADAMO experimental data [19]. It allows users to generate cosmic-ray (CR) muons based on custom parametrizations of their differential flux, i.e., Gaisser distribution. In ECoMuG, the following distribution is used:

$$J'_z \equiv \frac{dN}{dt dp d\theta d\phi dS_z} = \left[ 1600 \left( \frac{p}{p_0} + 2.68 \right)^{-3.175} \left( \frac{p}{p_0} \right)^{0.279} \right] \cdot (\cos \theta)^{n+1} \cdot \sin \theta \cdot \frac{1}{m^2 s sr GeV/c} (3.1)$$

ECoMuG is capable of generating muons from various topological surfaces, including spherical, hemispherical, cylindrical, and flat surfaces. This study uses a flat sky generator. In the flat sky generation, the origin position of generated CR muons is uniformly distributed over the generation surface. The azimuth angle  $\phi$  is uniformly randomly generated in  $[0, 2\pi]$ , and the momentum and zenith angle  $\theta$  are sampled from the differential flux in the above equation. Energy distribution peaks around 5.1 GeV, and zenith angle distribution follows  $\cos^2 \theta$ . CR muons flux is uniformly dependent on the azimuthal angle  $\phi$ . In addition, the ratio of the number of positive muons to the number of negative muons is  $\approx 1.28$  [20]. All the results are shown in Figures (3.1-3.4). The following are the parameters for ECoMuG.

Input Parameters	Output Parameters
Shape (flat), position ( $0, 0, -30$ mm) and size ( $160 \times 160$ mm $^2$ ) of generator surface.	Flat sky surface generator is located in the provided position.
Range of $\theta$ (Zenith angle) is $[0, \frac{\pi}{2}]$ radian and $p$ (momentum) $> 100$ MeV.	Distribution of $\theta$ and $p$ as per Equation 3.1 and outputs are shown in Figure (3.1-3.4).
Particle definition of positive and negative muons.	Number of positive and negative muons.

Table 3.1: Input and Output Parameters of Ecomug Generator.

### 3.1.1 Zenith angle distribution of cosmic ray muons simulated using ECoMuG

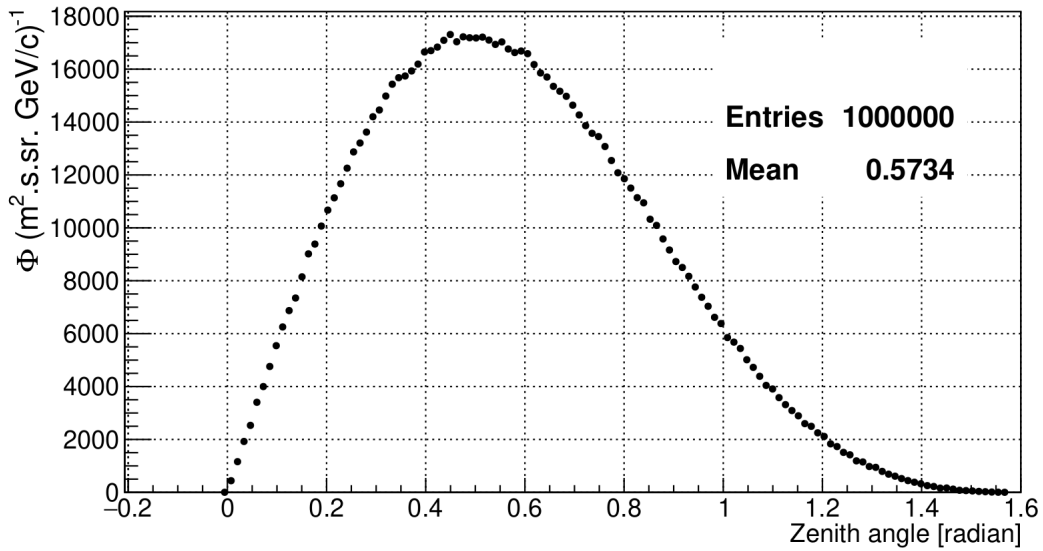


Figure 3.1: Cosmic Ray Muon zenith angle distribution generated using ECoMuG.

Figure 3.1 shows the zenith angular distribution of cosmic ray muons generated using ECoMuG. The zenith angle distribution follows  $\cos^2 \theta$ , which is expected for cosmic ray muons. The zenith angle is between the incoming cosmic ray muon and the vertical direction. It is measured from 0 to  $\pi/2$  radians.

### 3.1.2 Energy distribution of cosmic ray muons simulated using ECoMuG

Figure 3.2 shows the energy distribution of cosmic ray muons generated using ECoMuG. The energy distribution peaks around 5.1 GeV, which is expected for cosmic ray muons. It should be noted that the energy distribution is not uniform, and it follows the distribution given in Equation 3.1. The X-axis of the plot is logarithmic, and the Y-axis is linear.

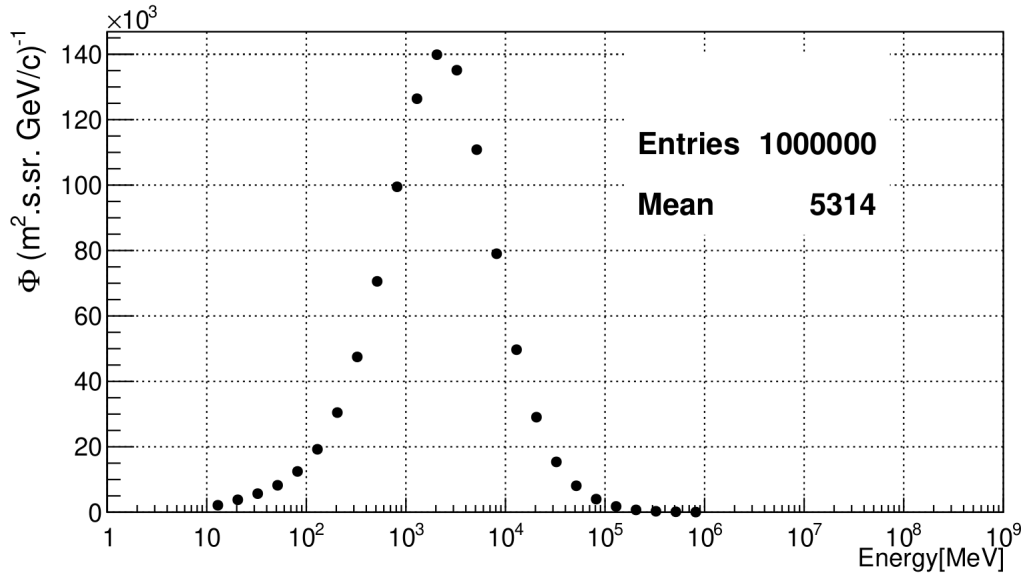


Figure 3.2: Cosmic Ray Muon energy distribution generated using ECoMuG.

### 3.1.3 Charge distribution of cosmic ray muons simulated using ECoMuG

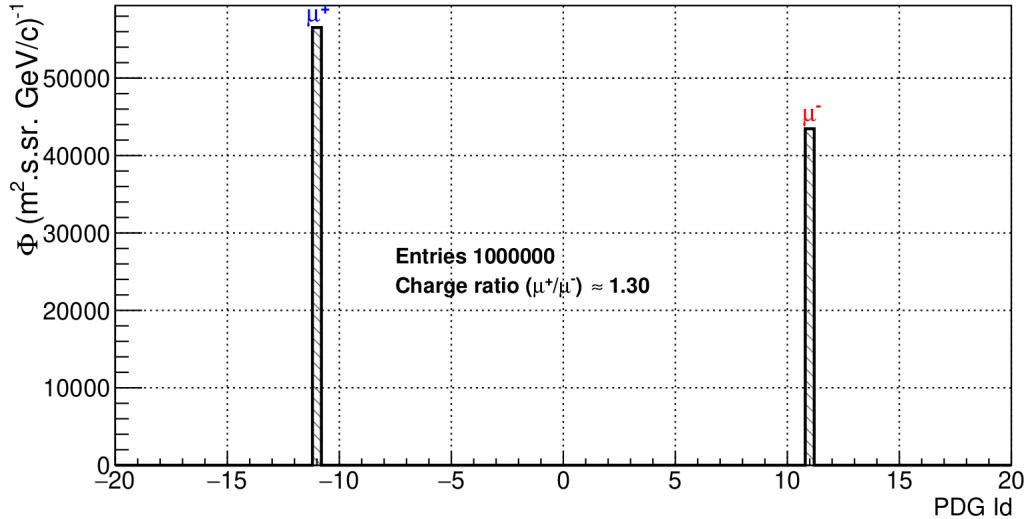


Figure 3.3: Cosmic Ray Muon charge distribution generated using ECoMuG.

Figure 3.3 shows the charge distribution of cosmic ray muons generated using ECoMuG. PDGID 13 represents the muon, and PDGID -13 represents the anti-

muon. It can be seen that the ratio of the number of positive muons to the number of negative muons is  $\approx 1.30$ , which is quite closer to the experimental value of 1.28 [20].

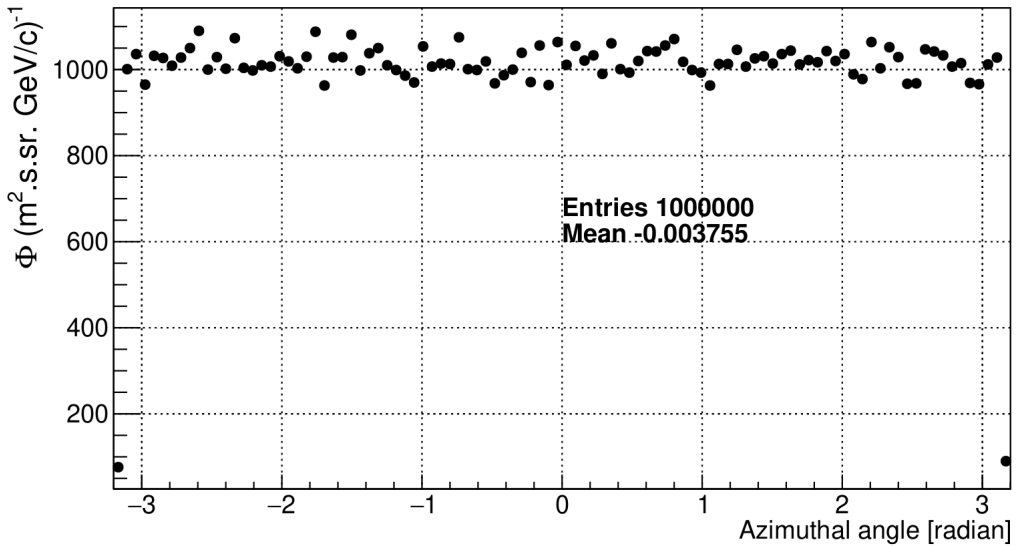


Figure 3.4: Cosmic Ray Muon azimuth angle distribution generated using ECoMuG.

Figure 3.4 shows the azimuth angle distribution of cosmic ray muons generated using ECoMuG. The azimuth angle is the angle between the incoming cosmic ray muon and the horizontal direction. It is measured from  $-\pi$  to  $+\pi$  radian. The azimuth angle distribution is uniform, as observed in the experimental data [19].

## 3.2 Simulation setup

Muoscope<sup>1</sup> geometry is built using GEANT4 toolkit [18]. GEANT4: GEometry ANd Tracking (GEANT4) toolkit. It is a software toolkit for the simulation of the passage of particles through matter. GEANT4 uses different physics lists for the simulation of particles. In this study, the FTFP\_BERT physics list is used.

---

<sup>1</sup>Muoscope is a term used for muon telescope.

- FTFP\_BERT is a physics list recommended by Geant4 for high energy physics (HEP) simulations.
- It includes all standard electromagnetic (EM) processes.
- For hadrons with energies less than 5 GeV, it works with the BerGni-style cascade model [21].
- For high-energy scenarios (greater than 4 GeV), it utilizes the FTF (Fritiof) model [22].

### 3.2.1 Muoscope geometry

The following are the key features of the Muoscope geometry:

- The Muoscope comprises four Resistive Plate Chambers (RPCs). The upper two RPCs are designed to track incoming muons, while the lower two track outgoing muons after they scatter through the target.
- Each RPC has an active area of  $160 \times 160 \text{ mm}^2$  and is housed within an acrylic box. The dimensions of the box are  $400 \times 400 \times 55 \text{ mm}^3$ , which are the proposed dimensions for a realistic telescope.
- Each RPC is made up of two graphite-coated glass plates.
- A Printed Circuit Board (PCB) panel with 16 readout strips is mounted on each electrode. The strips on the first electrode are arranged orthogonally to those on the second electrode.
- Each strip measures 9 mm in width and 160 mm in length. There is a 1 mm gap between consecutive strips.
- For a visual representation of the described setup, refer to Figure 4.1.

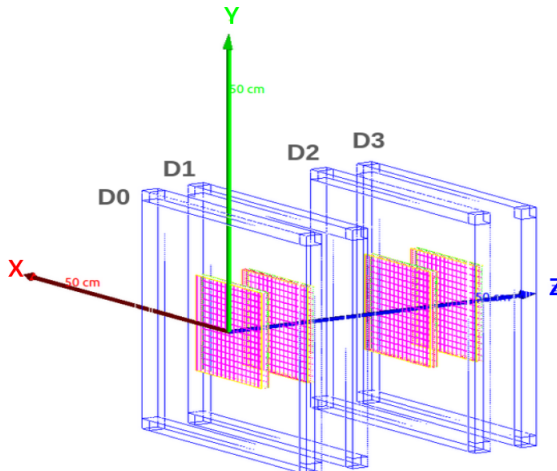


Figure 3.5: Muon telescope simulated with GEANT4.

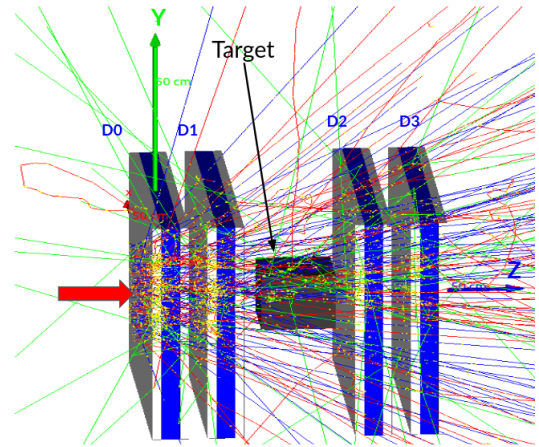


Figure 3.6: Simulated muon tracks across the muon telescope.

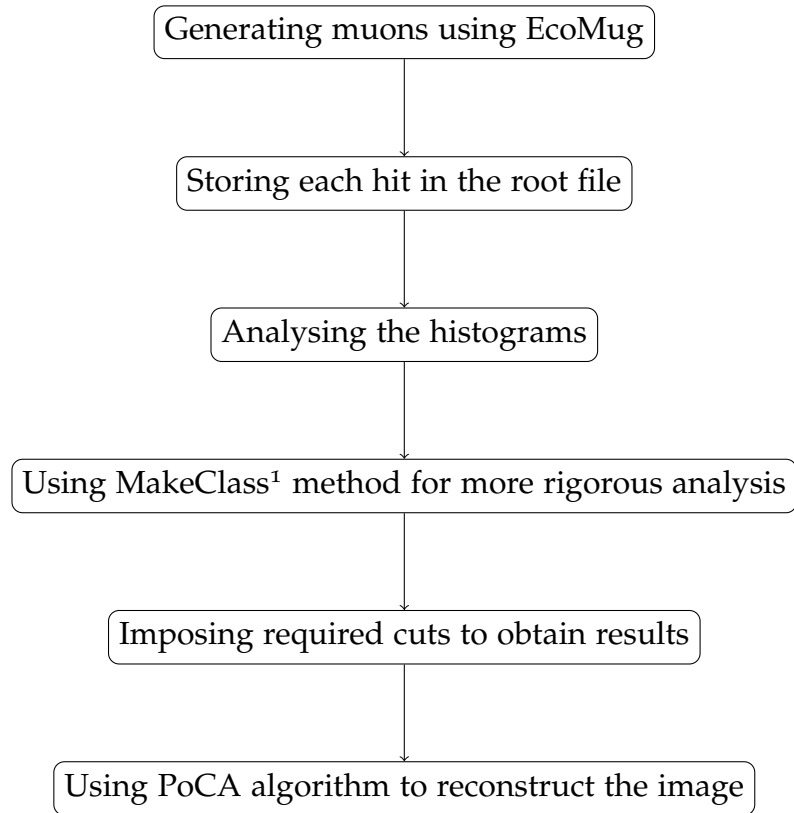
The geometry is simulated with GEANT4 of the muon telescope is shown in Figure 3.5. The muons are generated using EcoMug from 50 mm above the top layer of RPC (red pointer) and the area the generator is  $160 \times 160 \text{ mm}^2$ . The simulated muon tracks across the muon telescope are shown in Figure 3.6. The negative muon tracks are represented in red, the positive muon tracks in blue, and the green tracks depict secondary particles generated through the scattering of muons.

Following are the basic steps used to simulate a geometry in GEANT4.

- The abstract base class `G4VUserDetectorConstruction` is utilized to construct the geometry, creating a derived class named `DetectorConstruction`.
- The `Construct()` method is implemented within the `DetectorConstruction` class.
- All required materials are constructed using `G4Material`. It should be noted that some materials are readily accessible in the NIST manager[23].

### 3.3 Analysis pipeline

The analysis pipeline simulating the muography is shown in the flowchart below. The data stored is analyzed using CERN ROOT [24]. ROOT is a data analysis framework that provides a wide range of tools for data analysis, including histograms, graphs, and fitting. The pipeline consists of the following steps:



### 3.4 Optimizing of the Muoscope geometry

The geometry of the muoscope is shown in Figure 3.5. It consists of four RPCs, each with an active area of  $160 \times 160 \text{ mm}^2$ . The distance between the upper and lower RPCs must be optimized to achieve the best possible resolution. Do and D<sub>3</sub> are called outer detectors, while D<sub>1</sub> and D<sub>2</sub> are referred to as inner detectors. First, the distance between the Do-D<sub>1</sub> and D<sub>2</sub>-D<sub>3</sub> is optimized keeping the D<sub>1</sub>-D<sub>1</sub>

distance constant.

In Figure 3.7, in each detector, a hit is stored as  $X_{\text{hit}}$ . Then, a hit is removed from detector 1. A straight line is fitted using the remaining three hits, obtaining a hit value from the fitted track, denoted as  $X_{\text{fit}}$ . The residual is calculated as follows: Residual =  $X_{\text{hit}} - X_{\text{fit}}$ . In the XZ plane, each hit is labeled by the variables  $x_0, x_2$ , and  $x_3$ . Using these variables as independent parameters and their corresponding  $z_0, z_2$ , and  $z_3$  variables, we will perform linear regression to fit a track  $z = mx + c$  using the following coefficients:

$$m = \frac{n(\sum xz) - (\sum x)(\sum z)}{n(\sum x^2) - (\sum x)^2} \quad \text{and} \quad c = \frac{\sum z - m(\sum x)}{n} \quad (3.2)$$

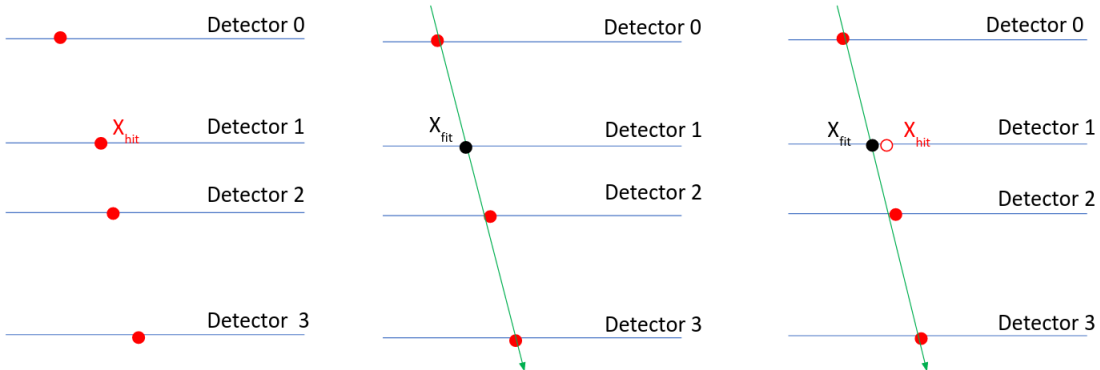


Figure 3.7: Illustration for determining the spatial resolution.

If these residuals are plotted, the distribution is observed to be Gaussian (figure 3.9). The hit position resolution ( $\sigma$ ) can be determined from the spread of the Gaussian distribution: Hit (position) resolution =  $\sigma(\text{Residual})$ .

Angular resolution is evaluated by recording hits in the upper trackers and extrapolating a line  $\mathbf{d}_0\mathbf{d}_1$ . Similarly, for lower tracker extrapolating a line  $\mathbf{d}_2\mathbf{d}_3$ , then using the dot product, we can compute the scattering angle between these two lines  $\mathbf{d}_0\mathbf{d}_1 \cdot \mathbf{d}_2\mathbf{d}_3 = \|\mathbf{d}_0\mathbf{d}_1\| \times \|\mathbf{d}_2\mathbf{d}_3\| \cos(\theta)$

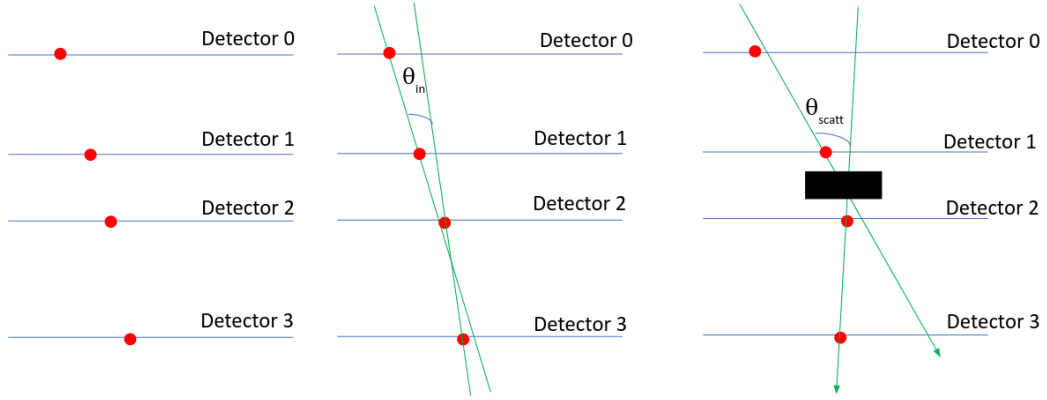


Figure 3.8: Illustration for determining the scattering angles distribution.

Where  $\theta$  is calculated as following

$$\theta = \arccos\left(\frac{\mathbf{d}_0 \mathbf{d}_1 \cdot \mathbf{d}_2 \mathbf{d}_3}{\|\mathbf{d}_0 \mathbf{d}_1\| \times \|\mathbf{d}_2 \mathbf{d}_3\|}\right)$$

The angular resolution is determined by analyzing the distribution of scattering angles between the two tracks, following a Gaussian distribution. The detector's obtained spatial and angular resolutions can be applied to introduce noise into simulated data, enhancing its resemblance to actual experimental data. Furthermore, the angular resolution serves as an offset for the scattering angle measurement distribution. While ideally, there should be no scattering in the absence of objects, the presence of materials like the acrylic box results in finite scattering.

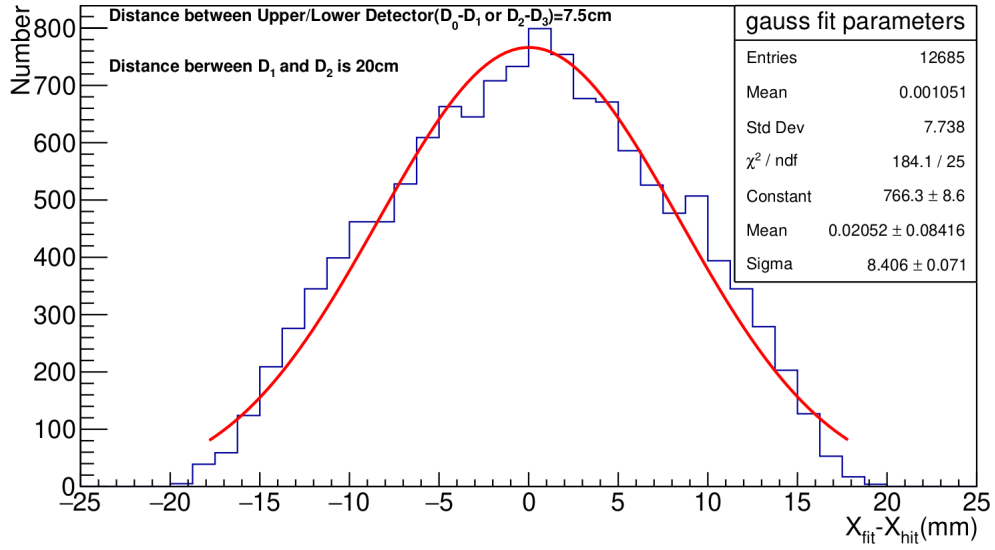


Figure 3.9: The residuals, resulting in a Gaussian distribution with a standard deviation of 8.41 mm.

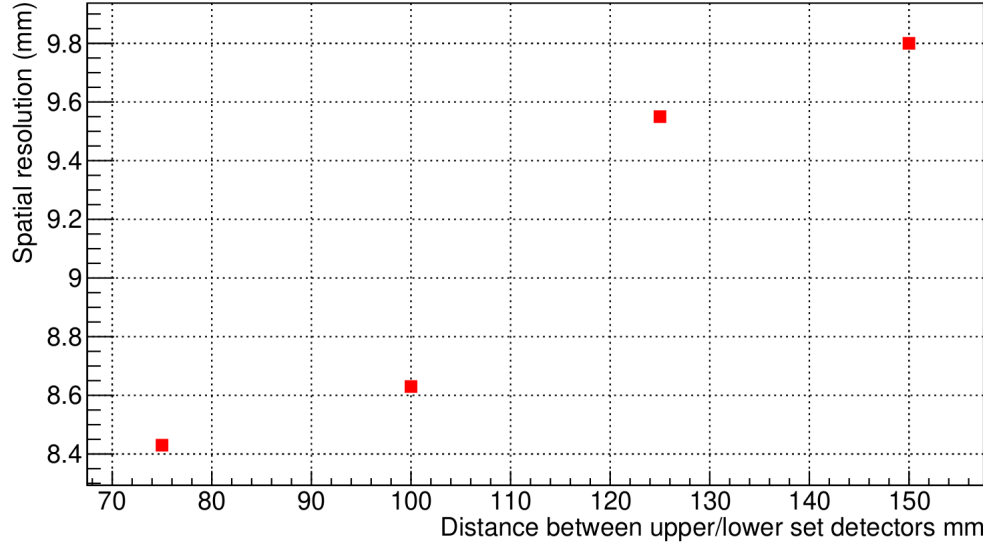


Figure 3.10: The spatial resolution as a function of the distance between the Do-D<sub>1</sub> and D<sub>2</sub>-D<sub>3</sub>.

Figure 3.10 shows the spatial resolution as a function of the distance between the Do-D<sub>1</sub> and D<sub>2</sub>-D<sub>3</sub>. The spatial resolution is observed to be inversely proportional to the distance between the detectors. The optimal distance between the detectors is determined to be 75 mm, as it results in the best spatial resolution.

### 3.4.1 Acceptance of the muon telescope

The acceptance of the muon telescope is defined as the fraction of muons that pass through the telescope. It is calculated using the following formula:

$$\text{Acceptance} = \frac{\text{Number of muons passing through all four layers}}{\text{Total number of muons generated}}. \quad (3.3)$$

The angular resolution of the muon telescope is defined as the minimum angle that the telescope can resolve. It is calculated using the following formula:

$$\text{Angular Resolution } (\sigma) = \frac{\Delta x \text{ (strip width)}}{\text{Distance between the detectors } (W)} \quad (3.4)$$

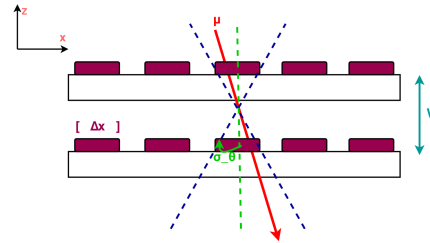


Figure 3.11: Schematic to show the calculation of angular resolution ( $\sigma$ ) [25] as a function of strip width and the distance between the detectors (D1 and D2) as shown in Figure 3.5.

Distance (w)(mm)	Acceptance(%)	Angular Resolution $\sigma$ (rad)
200	12.38	0.045
250	10.22	0.036
300	8.37	0.030
350	6.90	0.026
400	5.73	0.022
450	5.19	0.020
500	4.52	0.018
550	3.9	0.016
600	3.6	0.015

Table 3.2: Acceptance and angular resolution of muon telescope as a function of the distance between the D1 and D2 as shown in Figure 3.5.

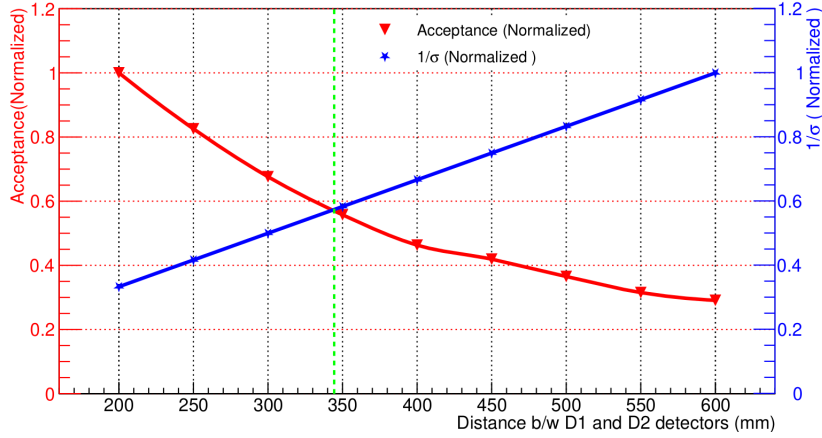


Figure 3.12: Acceptance of the muon telescope on the red axis and inverse of the angular resolution on the blue axis.

In Figure 3.12, the acceptance of the muon telescope and angular resolution are plotted as a function of the distance between the inner detectors. The best trade-off has been made between the acceptance and the angular resolution at an **optimum distance = 345 mm** between the inner detectors as shown in Figure 3.5. The acceptance is 8.37%, and the angular resolution is 0.026 rad.

### 3.4.2 Differentiating High-Z material using Muon Tomography

During the simulation, we positioned a lead(Pb, Z=82) block with dimensions of  $100 \times 100 \times 100$  mm<sup>3</sup>. Subsequently, we measured the deviation between the incoming and outgoing tracks in the XZ and YZ planes. The resulting distribution follows a Gaussian distribution, with the standard deviation ( $\sigma$ ) determined by Equation 1.6. For Lead radiation decay, the length is given by Equation (1.7), with an average momentum of approximately 5.2 GeV for atmospheric muons, and the standard deviation of the scattering angle is calculated to be 12.05 milliradians. The obtained result from the simulation is 12.34 mrad (see fig 3.14), which is closely aligned with the theoretical formula. This technique effectively distinguishes materials with higher atomic numbers (Z). Please see Appendix 4.3 for different types of

materials.

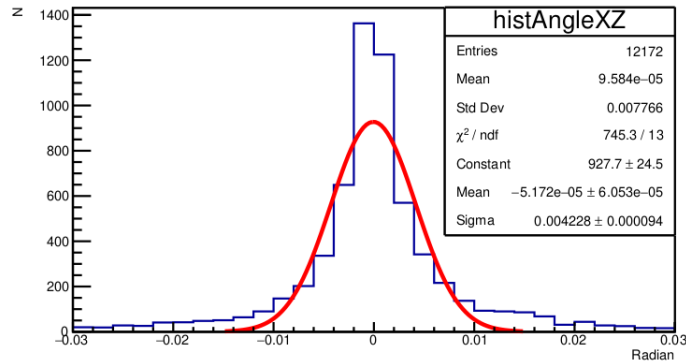


Figure 3.13: Scattering angle distribution without any target. The standard deviation is 4.2 mrad.

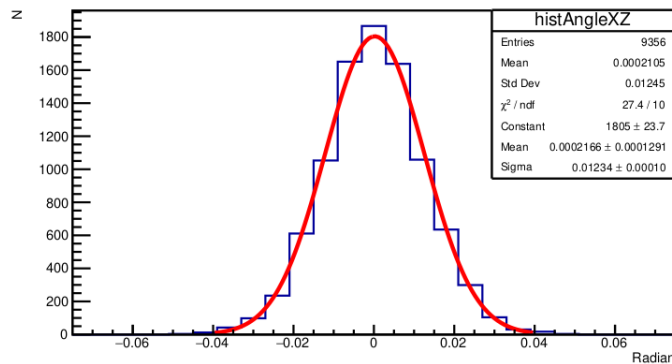


Figure 3.14: The scattering angle distribution for the lead block of  $100 \times 100 \times 100$  mm<sup>3</sup> size. The obtained standard deviation is 12.34 mrad, which is close to the theoretically calculated value as shown in Table 3.4.

Table 3.3: Properties of selected elements

Element	Atomic Mass (u)	Atomic Number (Z)	Density (g/cm <sup>3</sup> )	Radiation Length (cm)
Iron	55.8	26	7.87	1.76
Lead	207.2	82	11.34	0.56
Uranium	238.0	92	19.05	0.31

Table 3.4: Comparison of theoretically calculated using Equation 1.6 and simulated sigma values for different materials of thickness 100 mm.

Material (Z)	$\sigma_{\text{theoretical}}(\text{mrad})$	$\sigma_{\text{simulation}}(\text{mrad})$
Iron (26)	6.65	6.62
Lead (82)	12.05	12.34
Uranium (92)	16.82	16.60

Table 3.3 summarizes the properties of the selected elements. With the increase of the target material's atomic number (Z), the standard deviation in the scattering angle distributions increased. Table 3.4 shows the result of theoretically calculated values and simulated values, which are quite similar. Hence, by using the scattering angle distribution, the differentiation of high Z materials becomes feasible, considering that 1.6 is proportional to  $Z^2$ . It's important to note that this method demands prior knowledge of the target material's thickness, making it less practical in real-world scenarios. Nevertheless, its utility can be enhanced by incorporating Points of Closest Approach (PoCA) information through voxelization<sup>1</sup>.

## 3.5 Imaging: Point of Closest Approach (PoCA)

PoCA is discussed in detail in Section 2.4. Here implementation of PoCA is discussed. A Lead block of  $100 \times 100 \times 100 \text{ mm}^3$  is placed in between the upper and lower trackers as shown in Figure 3.6. PoCA is a simple algorithm that approximates the scattering point inside the material. The algorithm is based on the assumption that the muon scatters only once inside the material. It finds the mutual closest approach point of the muon incoming and outgoing tracks. But the presence of detector materials, like glass, acrylic, etc., gives false scattering points. To account for this issue, the following steps are implemented to improve

---

<sup>1</sup>The process of dividing 3D space into small voxels (cube) is called voxelization.

the reconstruction algorithm:

### 3.5.1 Scattering angle cut

- The algorithm is modified to consider only the specific range of scattering angle ( $\Delta\theta$ ) i.e  $\Delta\theta_{\min} < \Delta\theta < \Delta\theta_{\max}$ . This range is chosen because the low-momentum muons are more likely to scatter multiple times and effectively have a larger scattering angle. On the other hand, larger momentum muons are less likely to scatter multiple times and have a smaller scattering angle.

The following are the possible outcomes of the scattering angle:

1. If the scattering angle is small: (a) the point of interaction is a low-dense material or (b) muon has high momentum.
  2. If the scattering angle is large: (a) the point of interaction is a highly dense material or (b) muon has low momentum.
- To find the contribution of low-momentum muons in the scattering angle, a simulation is run without acrylic boxes and with acrylic boxes.

The scattering angle distribution without and with acrylic boxes, respectively, is shown in Figure 3.16 and 3.15. The scattering angle distribution with acrylic boxes is more spread out, indicating the contribution of low-momentum muons in the scattering angle. For imaging the target, a cut on the scattering angle is applied, which is obtained from the GEANT4 simulation. Only those POCA points are considered which have scattering angles less than  $\theta_{\max}$  cut given according to Figure 3.15. In addition, the muon telescope has an **acceptance of**  $\approx 7\%$ , in which a low zenith angle having low momentum [26] muon tracks are accepted. Which leads to the larger spread of scattering angle distribution.

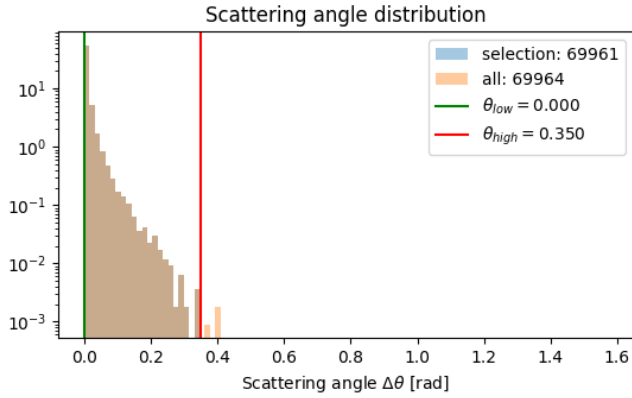


Figure 3.15: Without Acrylic boxes

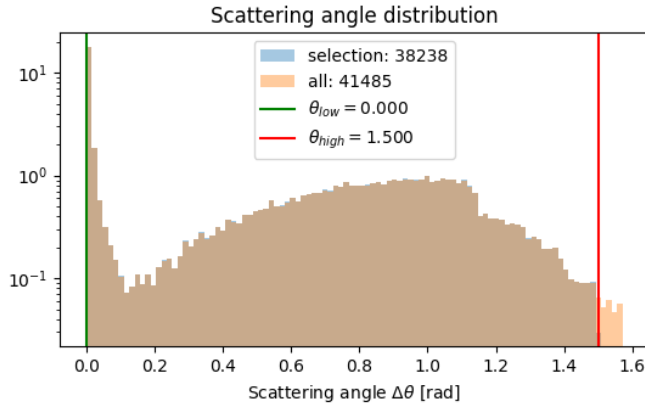


Figure 3.16: With Acrylic boxes

### 3.5.2 Voxelization of the 3D space

- The 3D space between the inner detectors as shown in Figure 3.5; is divided into small cubes ( $1000 \text{ mm}^3$ ) called voxels as shown in Figure 3.17.
- The POCA points and their scattering angles are stored in each voxel.
- Weight of each voxel is calculated using the POCA points and scattering angles according to Equation 3.7.

There are various methods to calculate the weight of each voxel, i.e., the mean of POCA points, RMS of scattering angles, etc. However, in this study, **Binned**

**Clustering Algorithm** is used to compute the weight of each voxel.

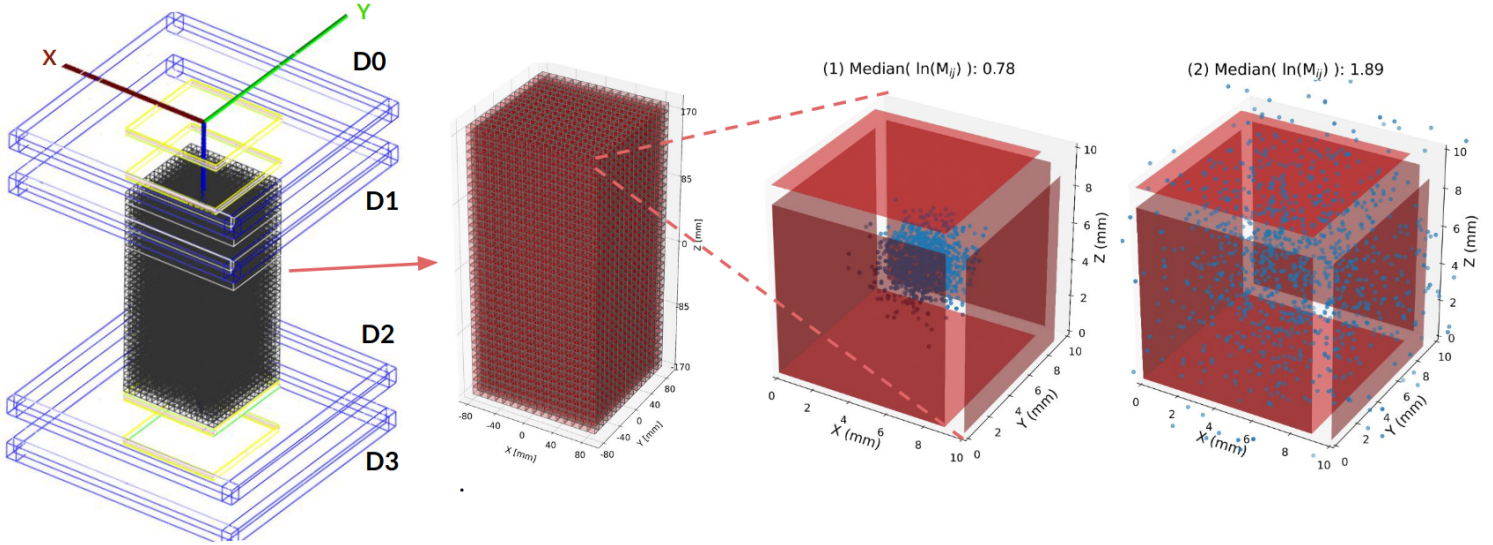


Figure 3.17: Demonstration of voxelization and BCA.

### 3.6 Binned Clustering Algorithm (BCA)

The Binned Clustering Algorithm (BCA) [27] is a method to calculate the weight of each voxel. The decision-making algorithm identifies the spatial clustering of muons that pass through high-Z target material. It breaks down the volume of interest into cubic voxels, sized to detect the intended targets. For the target of a Lead block with dimensions  $100 \times 100 \times 100 \text{ mm}^3$ , a Volume of Interest (VOI) of  $160 \times 160 \times 340 \text{ mm}^3$  is chosen. The algorithm computes a 'weighted clusteredness' value for each voxel.

For every pair of muon tracks with scatter vertices<sup>1</sup>  $v_i(x_i, y_i, z_i)$ ,  $v_j(x_j, y_j, z_j)$  located within the same voxel, the algorithm calculates a metric distance  $m_{ij}$  as shown in Equation 3.5.

---

<sup>1</sup>These vertices are scattering points computed using POCA algorithm.

$$m_{ij} = \|v_i - v_j\|. \quad (3.5)$$

This metric distance is then weighted by dividing it by the product of the scattering angles of the muons:

$$\tilde{m}_{ij} = \frac{m_{ij}}{\theta_i \cdot \theta_j} \quad (3.6)$$

where  $\theta_i$  is the scatter angle of muon i. The median of these logarithmic values of the metric is then computed and used as the voxel's final score.

$$\text{Score} = \text{Median}(\ln(\tilde{m}_{ij})) \quad (3.7)$$

This score is used to assign weight to each voxel, and plotting these voxels gives a reconstructed image of the target. The algorithm clusters POCA points in the region of interest based on their proximity, resulting in denser clusters for high-Z materials and, thus, smaller metric distances. It also factors in the muon scattering angle, with larger angles indicating high-Z materials and further reducing the score value (see Equation 3.7), and a lower score indicates high-Z material.

### 3.6.1 Parametrizing the accuracy of the BCA algorithm

For quantifying the accuracy of the BCA algorithm, A reference (true) 2D histogram is created, which has bins of size 100 mm<sup>2</sup>. Which contains the lowest score value (of reconstructed image) of each voxel in histogram bins numbered from x= 3 to 13 and y= 3 to 13. it mimics the 100 × 100 × 100 mm<sup>3</sup>. The Lead block and the rest of the bins are filled with 1 (highest value). The difference between the reference histogram and the reconstructed histogram is calculated, which will be used as an error. The error is calculated using the following method:

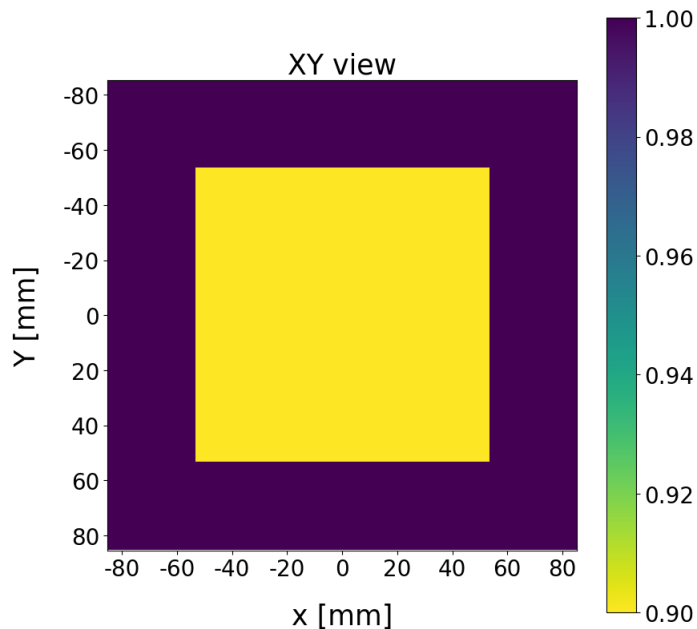


Figure 3.18: Reference histogram of a  $100 \text{ mm}^3$  Lead block.

```
# Assume true_hist and recon_hist are 2D arrays of size 16x16 representing
the reference and reconstructed histograms respectively.

# Calculate the difference between the two histograms to get the error
matrix. error_matrix = (true_hist - recon_hist)^2

# Calculate the mean of the error matrix to get the final error.
final_error = np.mean(error_matrix).
```

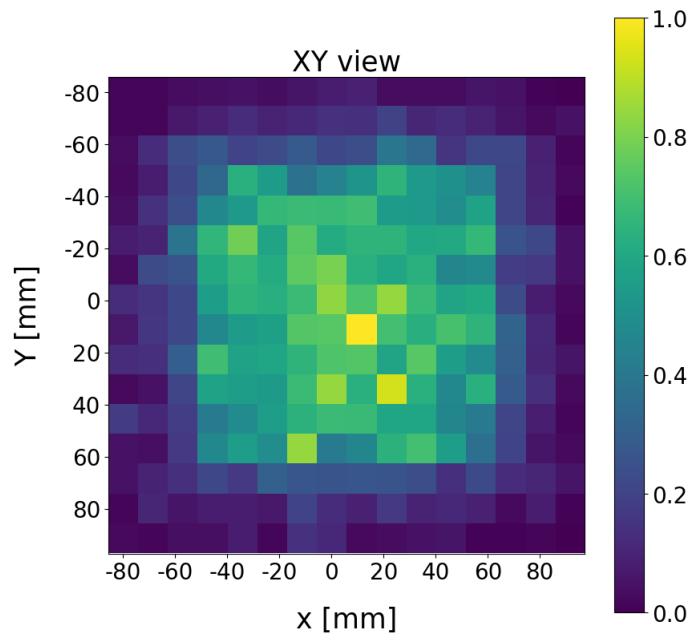


Figure 3.19: 2D image of  $100 \times 100 \times 100 \text{ mm}^3$  Lead block reconstructed with POCA algorithm (Error = 0.122).

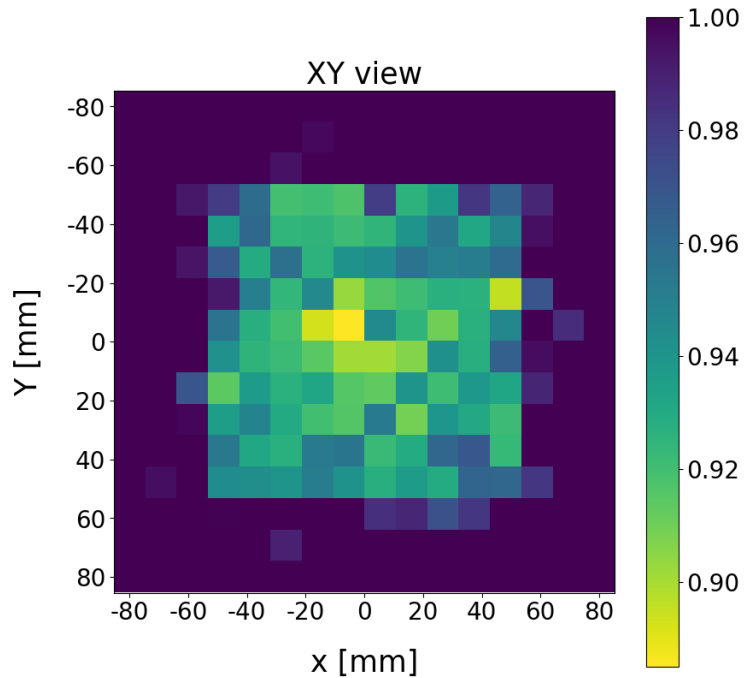


Figure 3.20: 2D image of  $100 \times 100 \times 100 \text{ mm}^3$  Lead block reconstructed with Binned Clustering Algorithm (Error = 0.002).

**NOTE:** In Figure 3.19 and 3.20 It is important to note that the color bars for both histograms are not identical. In the case of POCA, the color bar represents the number of POCA points (normalized) in each bin. Conversely, for BCA, the color bar indicates the normalized score as shown in Equation 3.7.

### 3.6.2 Input Parameters for BCA algorithm

The following are the input parameters for the BCA algorithm:

```
'n_max_per_vox:int' - Maximum POCAs in voxel metric computation.  
'n_min_per_vox:int' - Minimum POCAs in voxel metric computation.  
'dtheta_range:Tuple[float]' - Scattering angle cut in radian.  
'voxel_size:float' - Size of the voxel in mm.  
'volume of interest:Tuple[float]' - Volume of interest in mm.
```

In output, the algorithm returns a 2D histogram of the volume of interest with the Each voxel's score value can be used to reconstruct the target image.

## 3.7 Imaging Spent Nuclear Fuel Dry Cask with BCA

Spent nuclear fuel (SNF) is leftover radioactive material from nuclear reactors [28]. While it can't be used in reactors anymore, some of its parts could be used for weapons. It is stored in water pools near reactors, but that's not ideal. It's safer to move it to dry storage containers or special facilities. Since we don't have a permanent way to get rid of it yet, we might have to store it for longer than planned. Making sure none of this material goes missing or gets replaced with something else during storage is important. We need ways to check without opening the containers because that's costly and difficult. There Muon Scattering Tomography (MST) could be employed to image the SNF dry cask. The BCA algorithm is used

to reconstruct the image of the SNF dry cask.

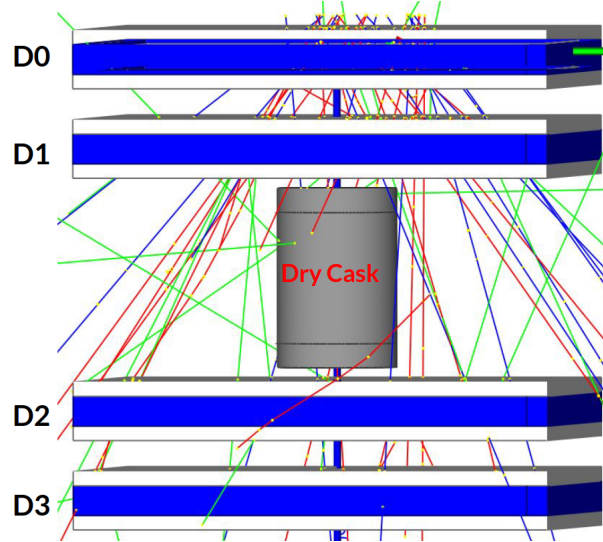


Figure 3.21: A dry Cask is placed in between detectors.

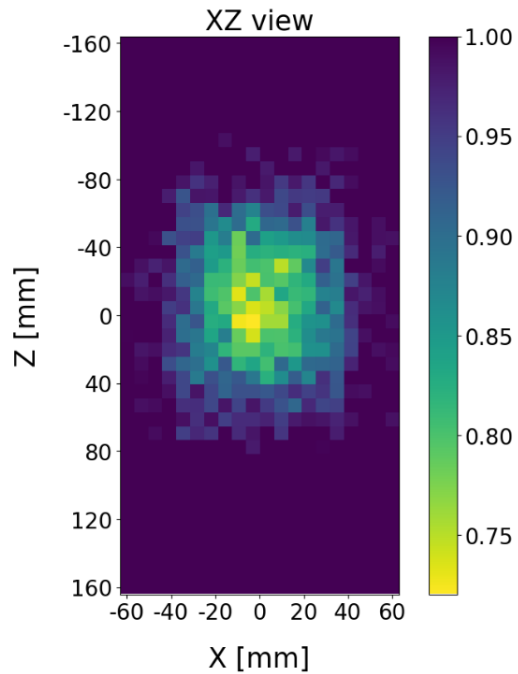


Figure 3.22: Shows a 2D image, an XZ projection, reconstructed using BCA. The presence of Uranium rods is visible in the center of the cask.

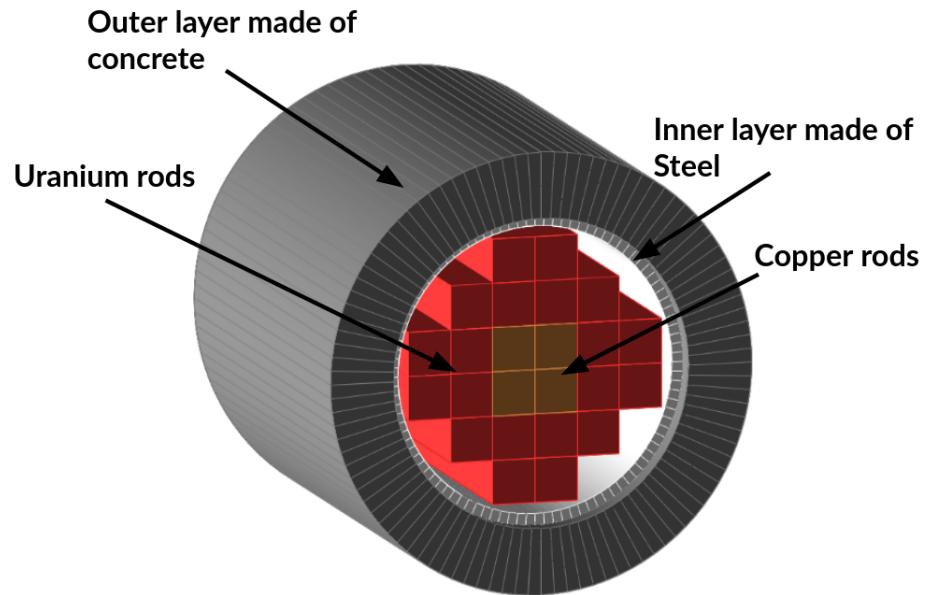


Figure 3.23: A dry cask made of concrete and steel containing Uranium (SNF) and copper rods is simulated in GEANT4.

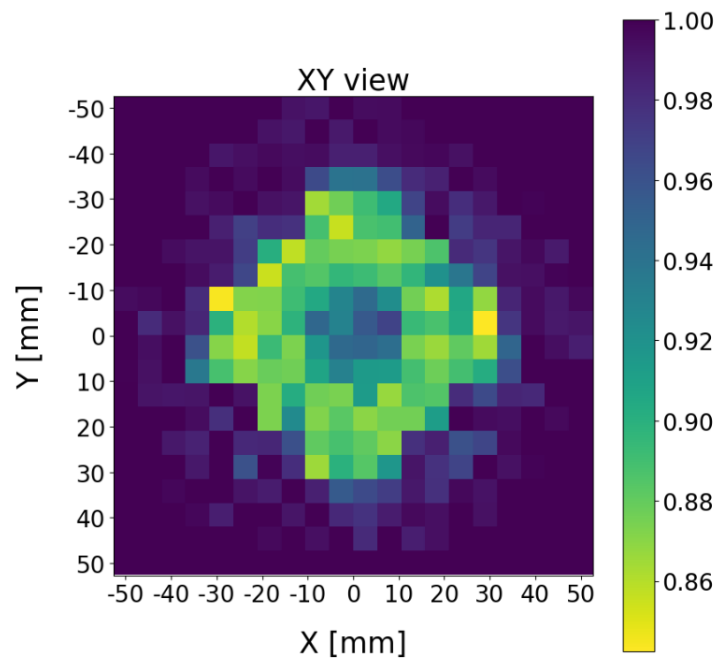


Figure 3.24: Presents the XY projection using the BCA reconstruction.

---

Component	Dimensions	Density(g/cm <sup>3</sup> )
Concrete Shell	Outer radius: 10 cm, Inner radius: 70 mm, Height: 110 mm	2.4
Steel Container	Outer radius: 7 cm, Inner radius: 65 mm, Height: 100 mm	7.8
Uranium Rods	20 rods, Each rod: 10x10x100 mm <sup>3</sup>	19.1
Copper Rods	4 rods, Each rod: 10x10x100 mm <sup>3</sup>	8.9

Table 3.5: Description of the Dry Cask components considered from the reference [29].

In Figure 3.22, the 2D image of the dry cask is reconstructed using the BCA algorithm. The XY projection of the dry cask is shown in Figure 3.24 and the XZ projection is shown in Figure 3.22. Missing uranium rods are visible in the XY projection. Copper rods and Uranium rods are differentiated in the reconstructed image. The BCA algorithm can differentiate between the high-Z material (Uranium) and the low-Z material (Copper) in the dry cask. The dry cask is successfully imaged using the BCA algorithm.

# Chapter 4

## Construction and characterization of Resistive Plate Chamber

In Chapter 3, simulation studies were conducted to image the interior of an object. As shown in Figure 3.5, the muon telescope consists of four detectors. Each detector is placed in an acrylic box. There are several options for choosing the detectors: scintillator, gas detector, and solid-state detector. This study uses a gas detector called the Resistive Plate Chamber (RPC). The RPC has a high spatial and time resolution and can detect muons [30]. In addition, the RPC is cost-effective and easy to fabricate. Before using the RPC as an active detector, it is important to understand its characteristics and performance. It will be used to detect the muon hits coordinates. This chapter deals with the experimental studies of the RPC.

### 4.1 Resistive Plate Chamber (RPC)

The Resistive Plate Chamber (RPC) is a gas detector that is widely used in high-energy physics experiments. It is invented by R. Santonico and R. Cardarelli in 1981 [31]. It consists of two parallel plates made of a high-resistivity material like Glass or Bakelite. These parallel plates are coated with graphite to apply high voltage. The plates are separated by a gas gap. The gas gap is filled with a gas mixture such as Tetrafluoroethane (R-134a), Isobutane, and Sulphur Hexafluoride. When a charged particle passes through the gas gap, it ionizes the gas molecules,

and the resulting electrons drift toward the anode and cathode plates. The electrons are accelerated in the electric field and ionize other surrounding atoms, resulting in generating more electrons and producing an avalanche of electrons. The avalanche of electrons will induce<sup>1</sup> a signal on the readout strips that could be read by the electronics. Since RPCs are easy to construct, have a fast response time, and better spatial resolution. RPC electrodes are highly resistive, making charge localized and providing accurate position information. It makes RPCs suitable for muon tomography studies. More details about the working principle of RPC are discussed in Appendix 4.1.

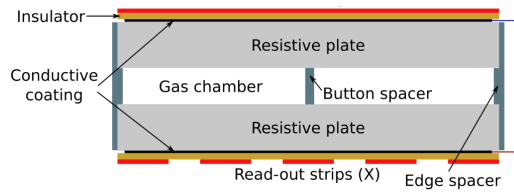


Figure 4.1: Design of a typical single gap RPC [32].

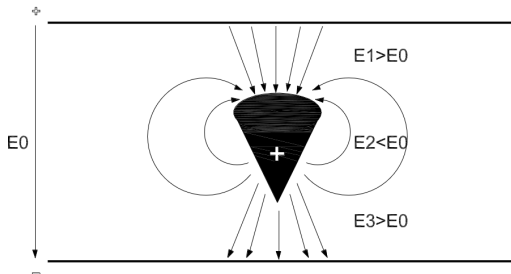


Figure 4.2: Avalanche formation inside the gas gap [33].

Figure 4.1 shows the typical single gap RPC design and 4.2 represents the schematic of an avalanche and the resulting electric field variations within the RPC.  $E_0$  is the uniform field applied across the electrodes, while  $E_1$ ,  $E_2$ , and  $E_3$

---

<sup>1</sup>Signals in the RPC are not created by collecting electrons. Instead, they are generated by the process of induction. That's why RPCs have a very fast time response, around 1 ns.

denote the effective fields at the avalanche charge distribution's tip, center, and tail, respectively.

## 4.2 Building the RPC and signal read-out panel

Two glass RPCs of similar size ( $200 \times 200 \times 3 \text{ mm}^3$ ) is built for developing a muon telescope. A printed circuit board (PCB) based on 16 strips of read-out panel is developed to read the RPC signals. Following are the steps used to build an RPC:

- Glass plates cleaned and coated with graphite paint for electrodes. Please see Figure 4.3b for the surface resistance map.
- Electrodes separated by acrylic and edged with spacers, sealed with epoxy.
- Gas nozzles added, assembly left to dry for a week.

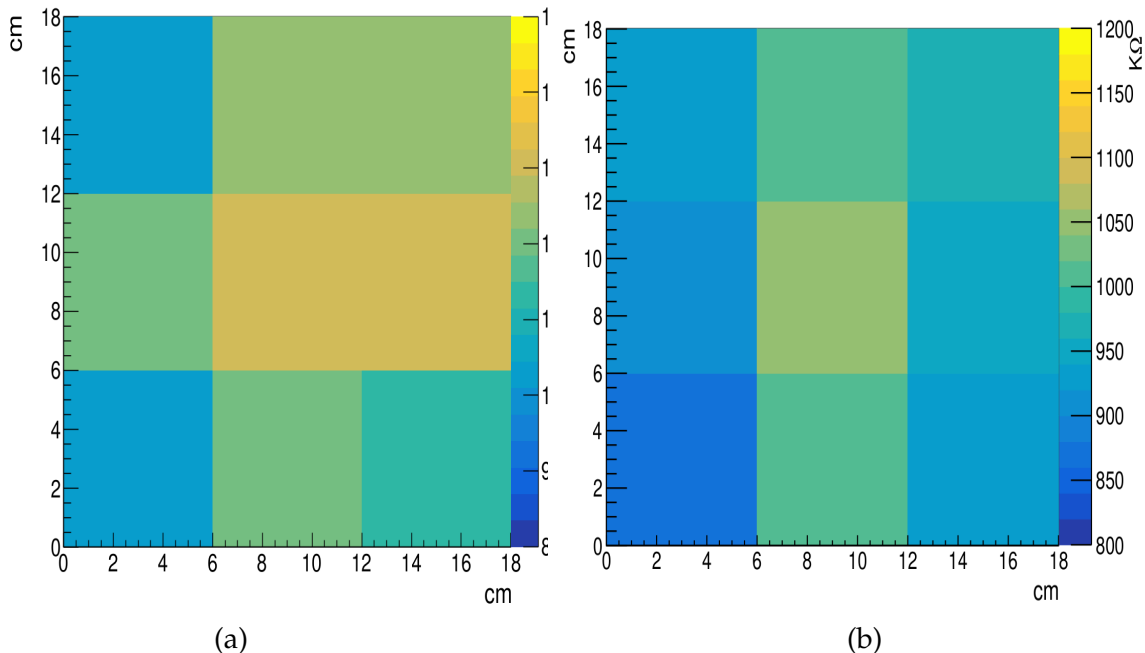


Figure 4.3: Surface resistance of graphite coated glass electrode (a) G5 and (b) G6.

A  $300\text{ mm} \times 300\text{ mm} \times 1.5\text{ mm}$  copper cladded PCB is etched with ferric chloride to develop copper strips. The copper strips are 9 mm in width and 230 mm in length.

- A design was printed with black ink on an A4 sheet. This sheet is placed on the PCB, and then the design is ironed on the PCB till printer ink is diffused on the PCB. It means the ink is transferred from the paper to the PCB.
- This PCB is placed inside the ferric chloride solution. The copper where ink is not deposited is etched out by the solution. The developed copper strip read-out panel is shown in Figure 4.4b.

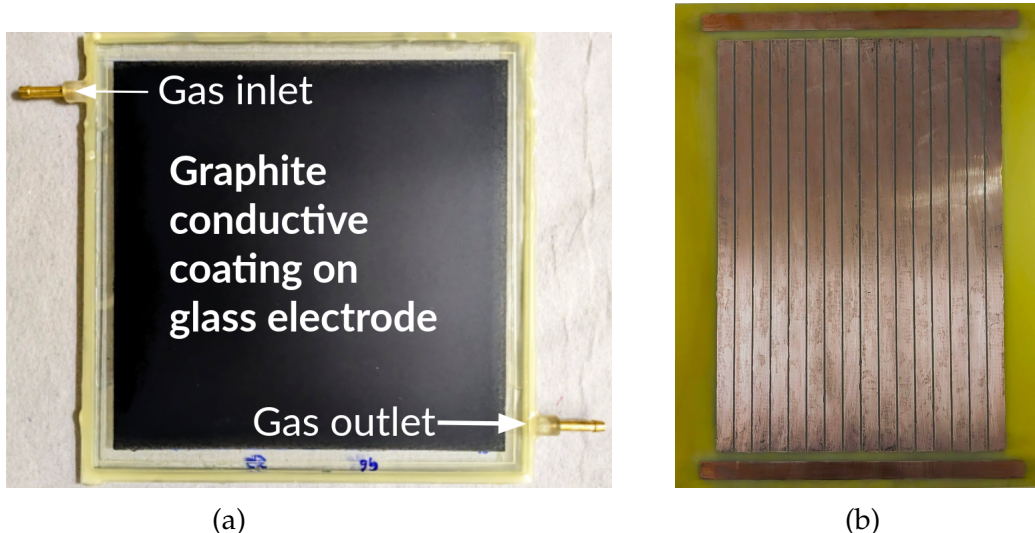


Figure 4.4: (a) A  $200 \times 200\text{ mm}^2$  glass RPC (b) A Printed Circuit Board (PCB) panel is used to develop 16 strips of copper read-out for reading the RPC signal.

Two glass RPCs are built, each with a size of  $200 \times 200\text{ mm}^2$ , as shown in Figure 4.4a. Two Printed Circuit Board (PCB) panels are developed to read the RPC signal. The PCB panel consists of 16 strips of copper read-out, as shown in Figure 4.4b.

### 4.3 RPC gas mixture

Gaseous detectors in proportional mode require sufficient primary ionization by the incident particle or radiation for a large signal via charge multiplication. Noble gases with lower ionization potential are commonly used. However, interaction with gas molecules can lead to photon emission, causing spurious avalanches and loss of proportionality and position resolution. To mitigate this, quench gases that absorb ultraviolet photons are used. Small amounts of highly electronegative gases are added to prevent streamer development and stabilize operations. The choice of gases and their proportions significantly affect detector characteristics. This study uses the following gas mixture:

- **R-134A ( $C_2H_2F_4$ ):** A freon variant with a large primary ionization cross-section and slight electronegativity is used for avalanche control.
- **Iso-butane ( $i-C_4H_{10}$ ):** A quencher absorbing photon energy kept below flammability limit due to combustibility.
- **Sulphur hexafluoride ( $SF_6$ ):** A strongly electronegative gas reducing streamer formation through electron attachment.

The gas mixture used consists of 95.3% R-134A, 4.5%  $i-C_4H_{10}$ , and 0.2%  $SF_6$ , as per the proportions mentioned in reference [32]. Furthermore, studies have been conducted to determine the optimal gas proportions for muography. In these studies, the concentrations of R-134A and  $SF_6$  were varied while keeping the concentration of  $i-C_4H_{10}$  constant. The objective is to identify the optimal operating voltage and gas mixture proportion that results in minimal charge collection and maximizes efficiency.

Following are the RPC responses that are calculated:

- **IV Characteristics:** The current-voltage (IV) characteristic curve is a plot of the current flowing through the RPC as a function of the applied voltage. The IV curve is used to determine the knee point and resistances of the RPC gas gap.
- **Efficiency:** The efficiency of the RPC is defined as the fraction of muons that pass through the RPC and produce a signal.
- **Charge collection:** RPC charge is the total charge induced on the readout strips.
- **Time resolution:** The time resolution of the RPC is defined as the time difference between the arrival of the muon at the RPC and the trigger signal.

#### **4.4 Current-Voltage (I-V) characteristics of glass RPC**

A 2 mm gas gap glass RPC ( $160 \times 160 \text{ mm}^2$ ). High voltage is applied across the graphite coating on the glass plates as shown in Figure 4.8. After varying the voltage applied from 1 kV to 12 kV, the current flow is recorded.

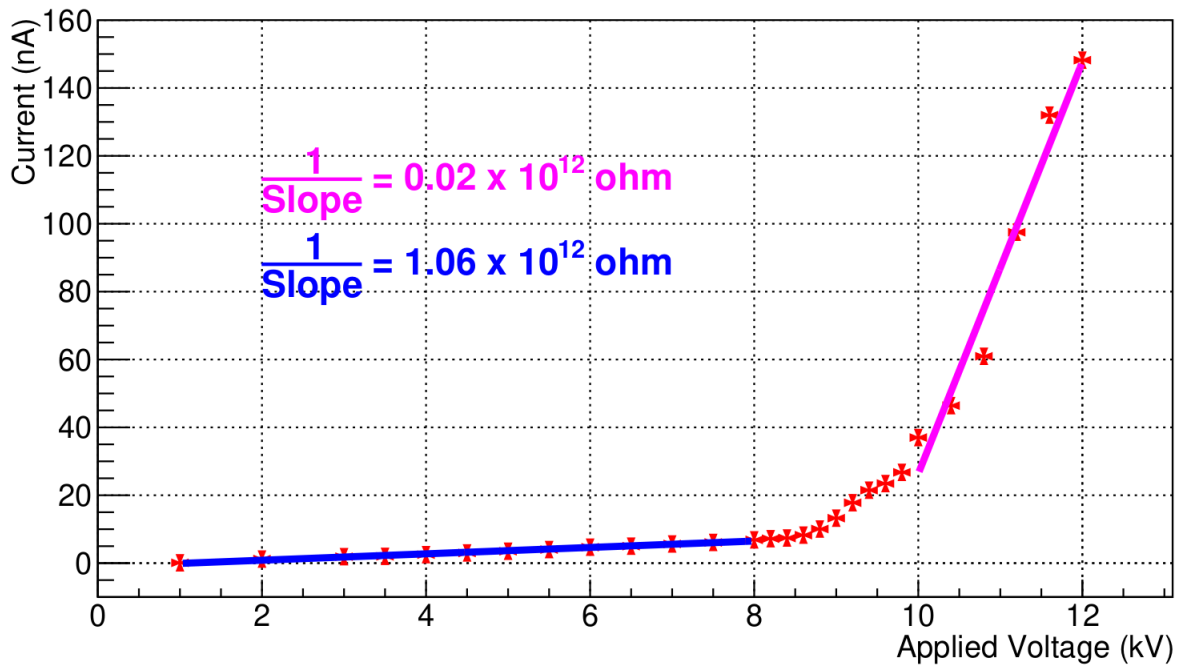


Figure 4.5: IV Characteristics of a glass RPC.

Figure 4.5 presents the IV characteristics of a glass RPC. 28 data points are recorded in two hours. Initially, the gas acts as an insulator, preventing current flow, with the only contribution coming from the acrylic spacer. As the voltage increases, the gas begins to ionize, allowing current to flow. The slope of the curve represents the reciprocal of the gas gap's resistance. This behavior is by Ohm's law, expressed as  $V = IR$ , where  $V$  is the voltage,  $I$  is the current, and  $R$  is the resistance. The resistance before the gas contribution is given by  $1.062 \times 10^{12}$  ohms, and after the gas starts to conduct; it becomes  $1.65 \times 10^{10}$  ohms.

## 4.5 Muon Telescope: Trigger Criteria

A muon telescope is built using three plastic scintillator detectors. This telescope sets up coincidence criteria for cosmic muon pulses from the glass RPC.

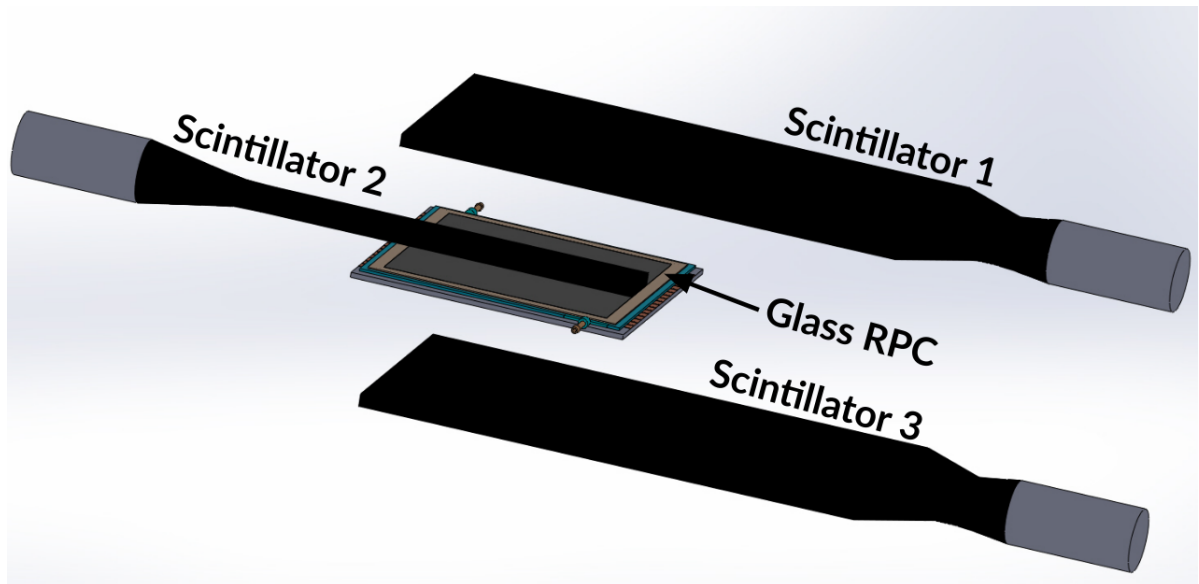


Figure 4.6: The muon telescope schematic comprises plastic scintillators, with Scintillators 1 and 3 of dimensions  $400 \times 200 \times 10 \text{ mm}^3$ , while Scintillator 2 dimensions  $300 \times 40 \times 10 \text{ mm}^3$ .

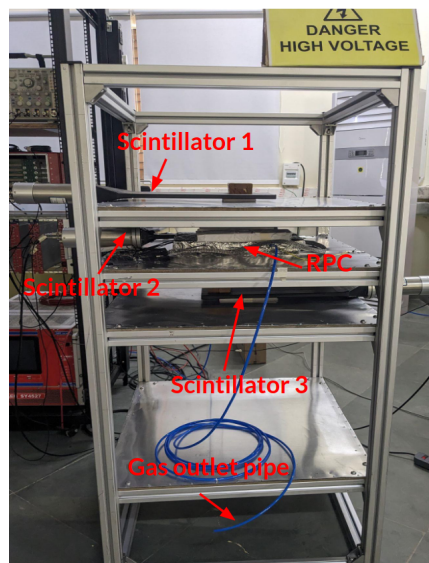


Figure 4.7: A muon telescope is used for measuring the efficiency of the glass RPC.

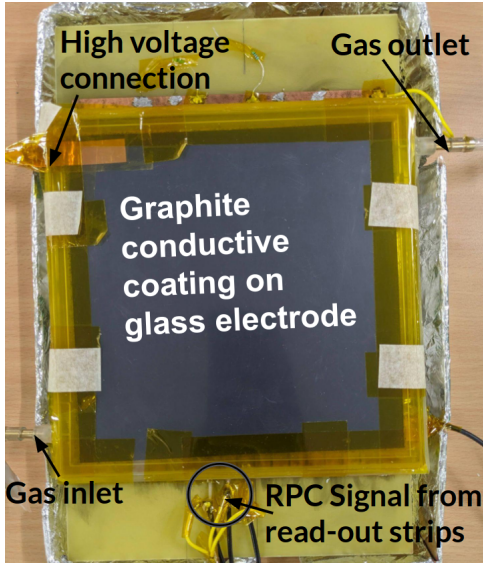


Figure 4.8: A  $200 \times 200 \text{ mm}^2$  glass RPC.



Figure 4.9: CAEN SY4527 power supply system is used for providing high voltage to the RPC.

Figure 4.6 shows the muon telescope schematic, comprising three plastic scintillators. Which is used to set up coincidence criteria for cosmic muon pulses from the glass RPC. Figure 4.7 shows the muon telescope used for measuring the efficiency of the glass RPC. Figure 4.8 shows a  $200 \times 200 \text{ mm}^2$  glass RPC, and Figure 4.9 shows the CAEN SY4527 power supply system used for providing high voltage to the RPC.

How it measures the efficiency of the RPC is explained below:

- Muons are identified by their ability to pass through the telescope's three layers of scintillators. If a charged particle is detected in all three layers, it's identified as a muon.
- The trigger pulse, represented by the coincidence of scintillator 1, scintillator 2, and scintillator 3, is referred to as the three-fold signal ( $\beta\text{F}$ ).
- A signal detected in the RPC coincides with the  $\beta\text{F}$  signal is classified as a

four-fold signal (4F). The coincidence is stretched to 100 ns to ensure the passage of muon.

- The efficiency of the RPC is calculated as the ratio of the number of 4F signals to the number of 3F signals.

## 4.6 RPC Efficiency Studies

As explained in previous sections, the efficiency of the RPC is defined as the ratio of the number of 4F signals to the number of 3F signals.

### 4.6.1 RPC signal

The RPC signal is the total charge induced [34] on the readout strips. An oscilloscope ( Tektronix MDO3024 ) is used to record the pulse. Data is acquired at the sampling rate of 2.5 Gs/s. The RPC signal is shown in Figure 4.10. RPC and trigger pulse are recorded in the CSV file format. These RPC pulses are analyzed offline using Python scripts.

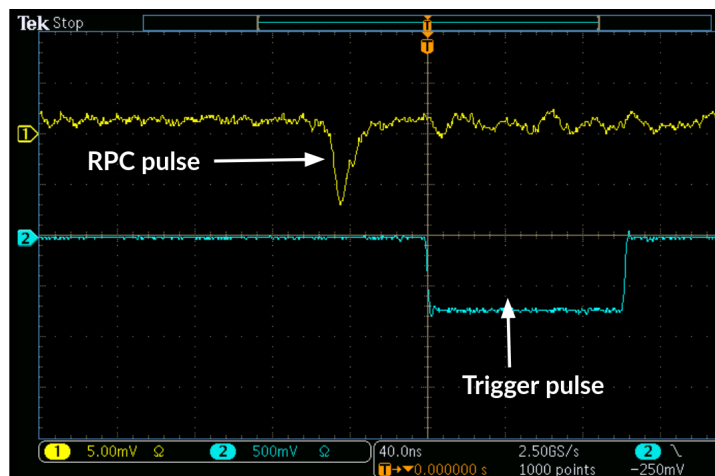


Figure 4.10: A RPC and trigger signal recorded by the oscilloscope.

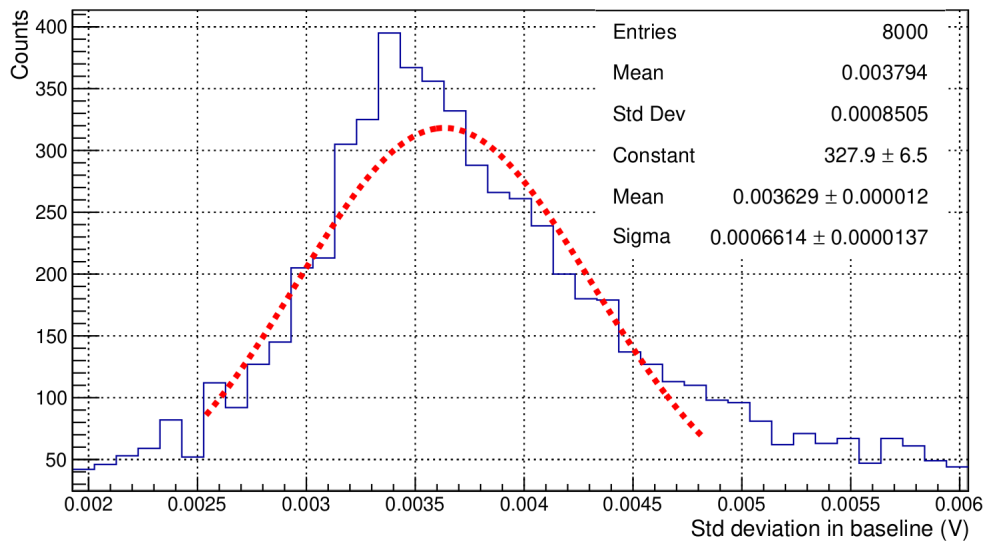


Figure 4.11: The threshold for the RPC pulse is set at  $5\sigma$  of the baseline noise.

Figure 4.10 and Figure 4.11 shows the RPC and trigger signal recorded by the oscilloscope and the threshold for the RPC pulse set at  $5\sigma$  of the baseline noise, respectively.

Both RPC and trigger signals are captured from the oscilloscope for offline analysis. A threshold for the RPC pulse is established by calculating the baseline noise, which is the signal fluctuation before the RPC pulse arrival. Out of ten thousand sampled points for each signal, the initial 250 are considered the baseline. The baseline standard deviation for each pulse is computed to form a distribution 4.11. The threshold for the RPC pulse is set at  $5\sigma = 3.3$  mV of this distribution. If RPC pulse amplitude exceeds this threshold (3.3 mV); it is considered a signal. For calculating efficiency, the following formula is used:

$$\text{Efficiency}(\%) = \left( \frac{\text{Number of signals above threshold}}{\text{Total number of signals}} \right) \times 100 \quad (4.1)$$

#### 4.6.2 RPC efficiency as a function of SF<sub>6</sub> concentration

In this study, a gas mixture (R134A:9.53, I-Butane:4.5, SF<sub>6</sub>:0.2) at 10 SCCM is flushed into the RPC, with varying SF<sub>6</sub> concentrations to examine its impact on RPC efficiency and charge collection. For each gas mixture tabulated in Table 4.1, a scan of efficiency is recorded at 16 voltage values from 8 kV to 11 kV in steps of 200 V. At each voltage, 1000 signals are collected along with the trigger, which took 1 hour, approximately. The aim is to minimize charge collection, as excessive collection can harm the electronics and increase the RPC's dead time. For muography, an RPC with an excellent spatial resolution (<9 mm) is required. However, RPCs with high charge collection have been observed to distribute charge across the readout strips. A smaller spread, hence lower charge collection, is preferred for better spatial resolution. In avalanche mode, the spread is around 4 mm in radius [35], and in streamer mode, it's 12 mm [36]. To reduce charge collection, SF<sub>6</sub> is added in proportions as listed in Table 4.1.

	R134A (SCCM)	I-Butane (SCCM)	SF <sub>6</sub> (SCCM)
Rate 1	9.55	0.45	0.00
Rate 2	9.53	0.45	0.02
Rate 3	9.50	0.45	0.05
Rate 4	9.47	0.45	0.08
Rate 5	9.53	0.45	0.10

Table 4.1: Flush rate of gases in Standard Cubic Centimeters per Minute (SCCM).

Roles of gases in the RPC gas mixture are discussed in section 4.3. The RPC efficiency is calculated for each gas mixture mentioned in Table 4.1. In Figure 4.12, efficiency is plotted as a function of the applied voltage for each gas mixture. The inclusion of SF<sub>6</sub> has notably decreased efficiency, and with an increase in SF<sub>6</sub> concentration.

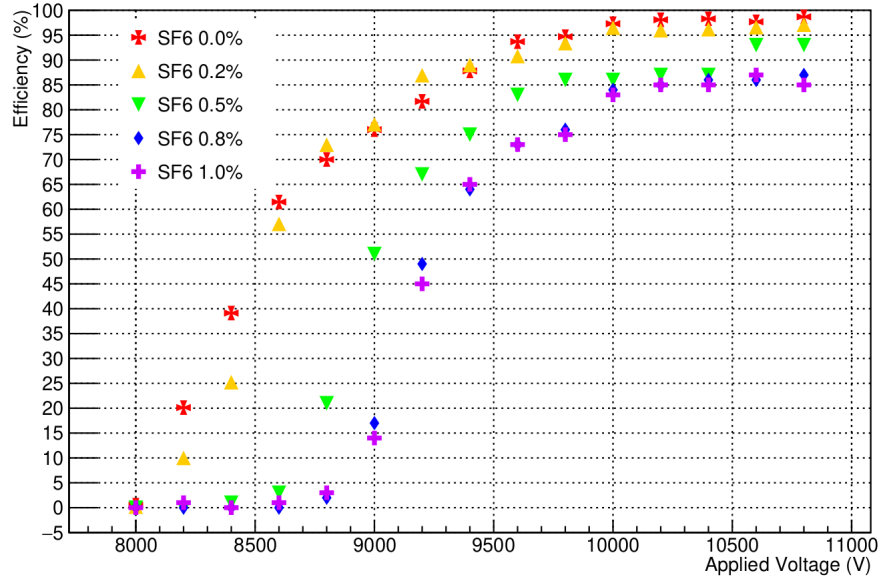


Figure 4.12: RPC efficiency as a function of SF<sub>6</sub> concentration and applied voltage.

## 4.7 Charge collection as a function of SF<sub>6</sub> concentration

After the RPC signal is captured, the charge collection is analyzed by integrating the RPC pulse is shown in Figure 4.10 in the time window of -100 ns to +100 ns.

$$\text{Charge} = \frac{1}{\text{Amplification factor}} \int_{-100 \text{ ns}}^{+100 \text{ ns}} \frac{\text{Voltage}}{\text{Resistance}} dt \quad (4.2)$$

In Equation 4.2, the resistance refers to the impedance of electronics used for signal collection. The amplification factor is the RPC signal's amplification by the CAEN Mod N979 fast amplifier. The voltage represents the RPC signal's height in fig 4.10. The integration is performed using Python's *scipy.integrate.trapezoid* library.

It is found from Figure 4.12 that if the applied voltage exceeds 10 kV, the RPC efficiency is above 85%. Hence, 10 kV is used as the operating voltage for charge collection studies. Additionally, charge collection is also studied at 10.2 kV and 10.4 kV for all gas mixtures listed in table 4.1.

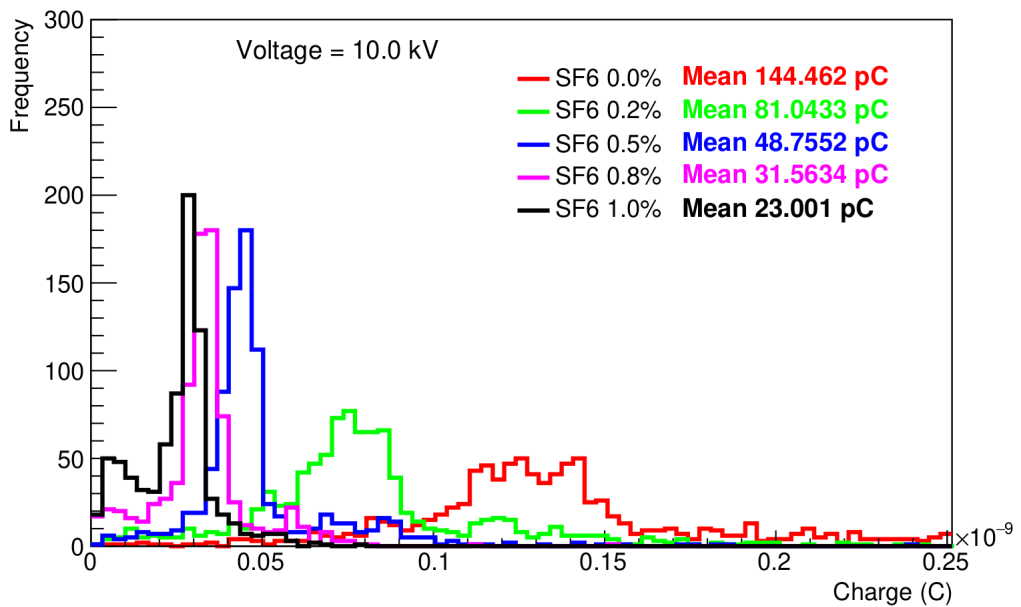


Figure 4.13: Charge spectra at 10.0 kV.

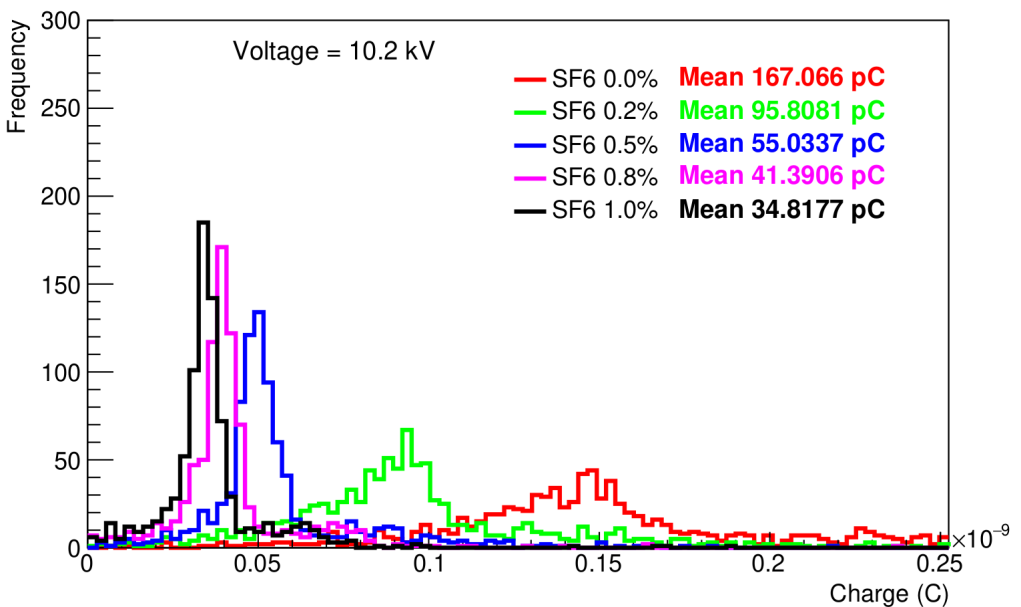


Figure 4.14: Charge spectra at 10.2 kV.

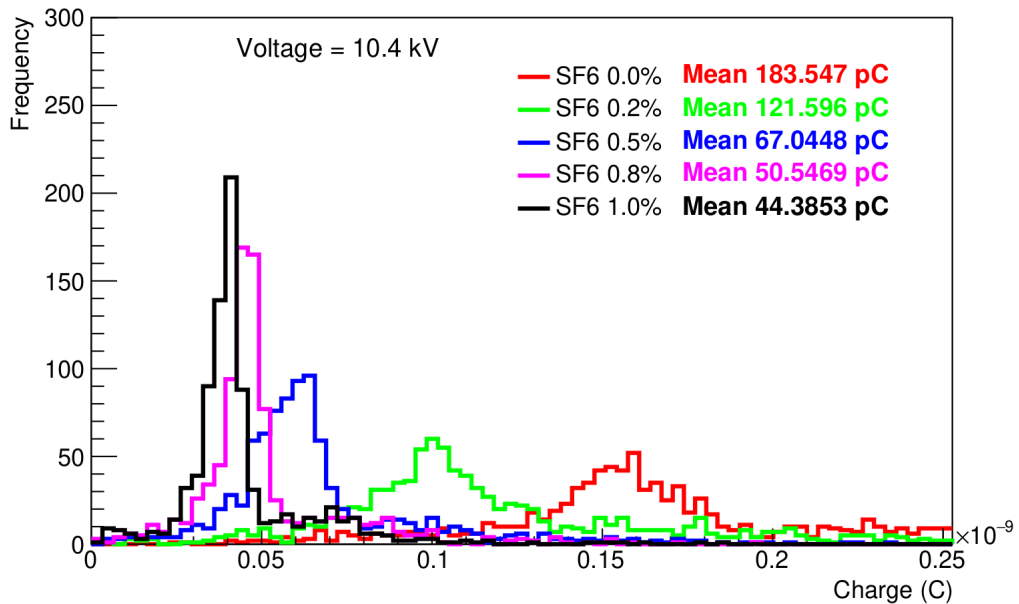


Figure 4.15: Charge spectra at 10.4 kV.

Figure( 4.13-4.15) shows the charge spectra for each gas mixture plotted at 10.0 kV, 10.2 kV, and 10.4 kV. It is shown that the charge collection decreases with an increase in SF<sub>6</sub> concentration. The peaks shift to the left side, with an increase in SF<sub>6</sub> concentration. Table 4.2 shows the efficiency and charge collection for different SF<sub>6</sub> concentrations at 10 kV, 10.2 kV, and 10.4 kV. Both efficiency and charge collection decrease with an increase in SF<sub>6</sub> concentration.

## 4.8 Time resolution of RPC

The time resolution of the RPC is defined as the standard deviation of the time differences between the 10% height of the RPC pulse as shown in Figure 4.10 and the trigger pulse. Figure 4.16 shows the time resolution of the RPC as a function of the applied voltage 10 kV and SF<sub>6</sub> concentration 0.5%.

Voltage (kV)	SF <sub>6</sub> Concentration (%)	Efficiency (%)	Mean Charge (pC)
10	0.0	97.3	144.47
	0.2	96.5	81.04
	0.5	86.5	48.76
	0.8	84.6	31.60
	1.0	83.1	23.00
10.2	0.0	98.1	167.07
	0.2	96.0	95.81
	0.5	87.51	55.03
	0.8	85.68	41.40
	1.0	85.28	34.82
10.4	0.0	98.29	183.54
	0.2	96.2	121.60
	0.5	87.0	67.04
	0.8	86.0	50.55
	1.0	85.68	44.38

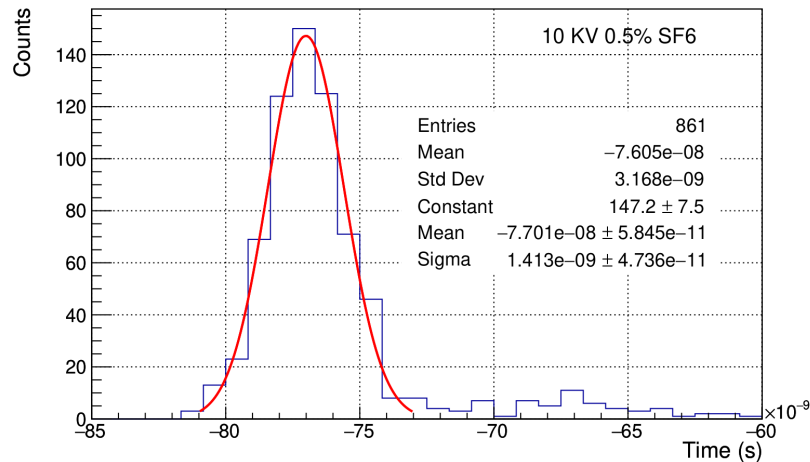
 Table 4.2: Efficiency and charge collection of RPC as a function of SF<sub>6</sub> concentration.


Figure 4.16: Time resolution of RPC.

Table 4.3 shows the time resolution of the RPC for different SF<sub>6</sub> concentrations. It is observed that the time resolution increases with an increase in SF<sub>6</sub> concentration. Since SF<sub>6</sub> is a strongly electronegative gas, it arrests avalanche development through electron attachment, effectively reducing streamer formation. However, this also increases the time resolution of the RPC. Similar findings were also noted in Section

3.9.1 of the thesis [33]. Since the rate of cosmic muons ( $100 \text{ Hz/m}^2$ ) [15] is quite low compared to collider experiments like CMS  $7.5 \times 10^4 \text{ Hz/m}^2$  [37]. Therefore, time resolution in the order of nanosecond is good for muography studies.

SF <sub>6</sub> (%)	Time Resolution (ns)
0.0	1.27
0.2	1.41
0.5	1.42
0.8	1.56
1.0	1.69

Table 4.3: SF<sub>6</sub> concentration and time resolution.

## 4.9 Relative humidity test on acrylic chamber

The efficiency of RPC remains relatively stable with changes in Relative Humidity (RH) at room temperature. However, at higher temperatures, RH does impact efficiency, as noted in [38]. Given that RPCs might be operated outdoors for muography studies, an acrylic chamber has been designed to shield the RPC from external temperature and humidity fluctuations.

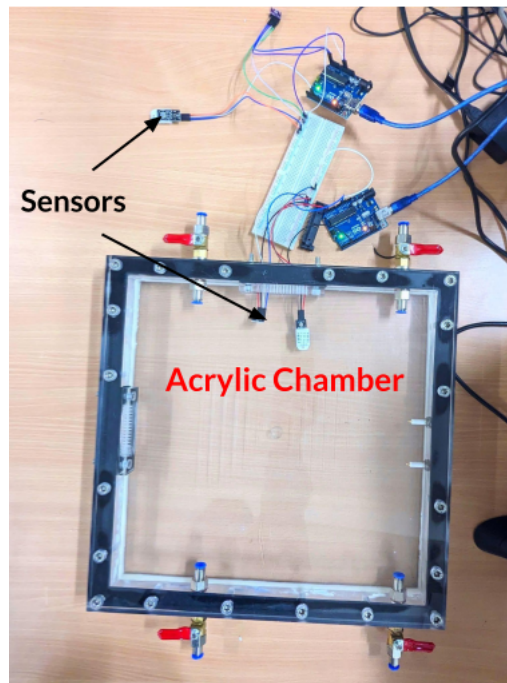


Figure 4.17: Acrylic chamber for housing the RPC.

An acrylic chamber is used in GEANT4 simulation as shown in Figure 3.5 and is designed to house the RPC. The chamber shown in Figure 4.17 is designed to be gas-tight and has a gas inlet and outlet for flushing the RPC with the gas mixture. The chamber is tested for humidity stability and gas tightness. Two BMP280 sensors are used to measure the humidity and temperature inside and outside the chamber. Humidity data is collected using the Arduino Uno microcontroller for 30 days and plotted in Figure 4.18.

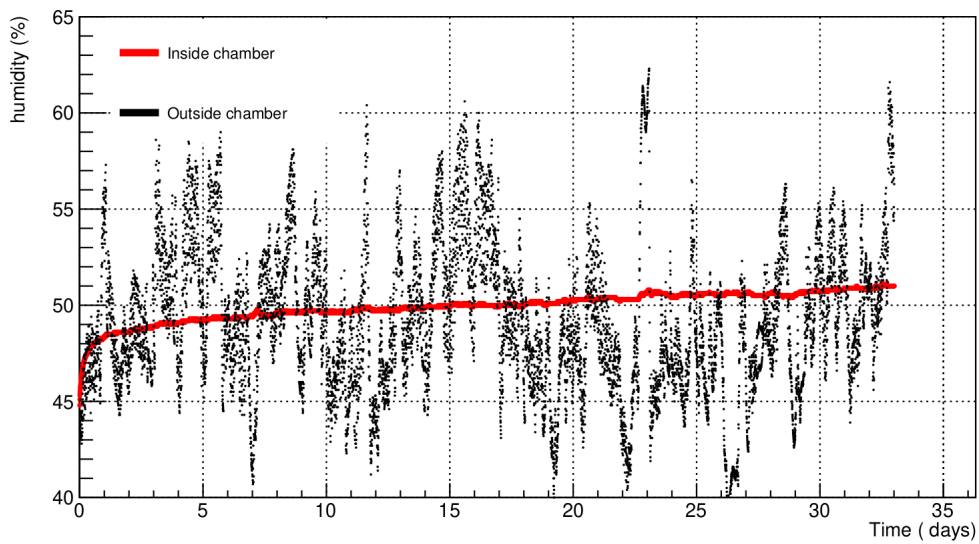


Figure 4.18: Humidity levels are monitored both outside and inside the acrylic chamber for 32 days. Red points represent humidity levels inside the chamber, while black points represent humidity levels inside the chamber.

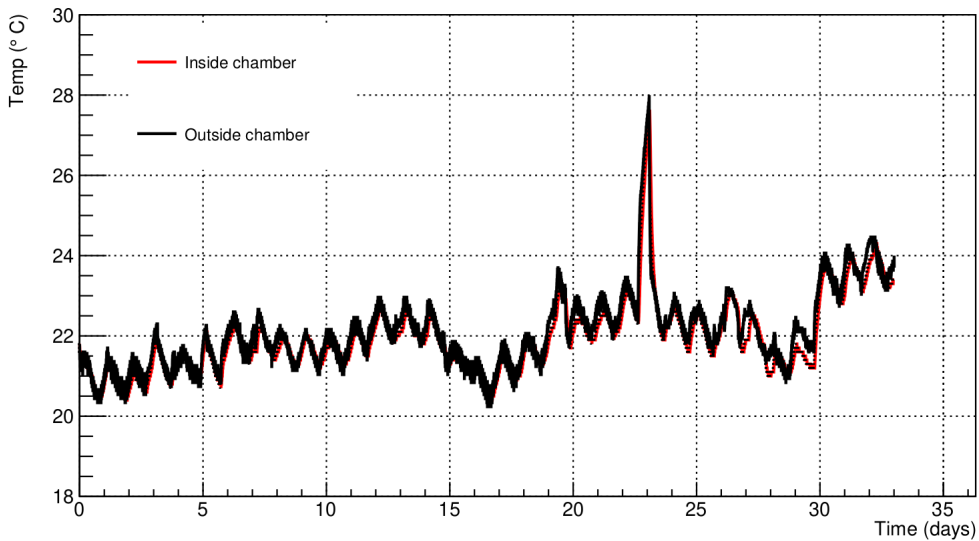


Figure 4.19: Temperature is monitored both outside and inside the acrylic chamber for 32 days. Red points represent temperature inside the chamber, while black points represent the temperature inside the chamber.

In Figure 4.18, the graph shows humidity levels over 15-minute intervals. Outside the chamber, humidity fluctuates significantly, while inside, it changes

gradually before reaching a stable level. Therefore, this chamber could be used to place RPC. Figure 4.19 shows the temperature inside and outside the chamber. The temperature inside the chamber and outside the chamber is almost the same since the chamber has valves for the gas inlet and outlet which are made of steel. The steel valves are good conductors of heat, which makes the chamber temperature the same as the outside temperature.

## **4.10 Summary and future prospects**

This project was focused on Muography studies using RPC. It contains both simulation and experimental studies. In the first part, a GEANT4 simulation was performed to image the interior of an object using PoCA. On top of that, PoCA is improved using voxelization-based algorithm like Binned Clustering Algorithm (BCA). In the second part, experimental studies were conducted to understand the RPC characteristics. The RPC efficiency, charge collection, and time resolution were studied as a function of SF<sub>6</sub> concentration. The RPC efficiency decreases with an increase in SF<sub>6</sub> concentration. The charge collection also decreases with an increase in SF<sub>6</sub> concentration. The time resolution of the RPC increases with an increase in SF<sub>6</sub> concentration. The acrylic chamber was designed to house the RPC and tested for humidity stability. The humidity and temperature inside and outside the chamber were monitored. The humidity inside the chamber was found to be stable. However, the temperature inside the chamber was found to be the same as the outside temperature.

### **4.10.1 Future prospects**

In the simulation, it is possible to consider clusterization of hits in the RPC to make it closer to the experimental setup. ASIC and FPGA-based DAQ system

can be implemented to read the pulses from all the RPCs channels of the muon telescope. This project studies the effect of SF<sub>6</sub> on RPC efficiency, charge collection, and time resolution. The effects of isobutane can be studied to operate the RPC in pure avalanche mode.

# Appendix A

## 4.1 RPC: Avalanche and Streamer

The Resistive Plate Chamber (RPC) is a gaseous detector. Charged particles or radiation ionize gas molecules in the RPC chamber, with ions and electrons moving toward the cathode and anode in an electric field. High enough fields cause secondary ionization. The total electron count is given by  $n = n_0 e^{(\alpha - \beta)x}$ , where  $n_0$  is primary electrons,  $\alpha$  is the first Townsend ( $\beta$ ) is the attachment coefficient (number of electrons captured by the electronegative gas molecules per unit length).

### 4.1.1 Avalanche Mode

When particles with high energy traverse the gas within the detector, they initiate the creation of primary electrons and ions. As these primary particles move under the influence of the applied electric field, they lead to additional ionizations. This chain reaction of ionization events, referred to as an avalanche, results in the induction of a current on the read-out strips of the detector. In this region, known as the proportional region, the charge that is produced is in direct proportion to the number of primary particles, and this relationship is governed by the gas gain ( $G$ ). For a low value of  $G$ , the charge that is generated is relatively small, necessitating amplification to produce signals that can be detected. The ability of

the RPC to manage a rapid influx of particles is attributed to the small magnitude of the charge it produces. The area of a discharge cell, which is determined by the total charge deposited, plays a significant role in the rate of detection of the RPC. To operate in the avalanche mode, a mixture of gases, specifically  $C_2H_2F_4$ ,  $i-C_4H_{10}$ , and  $SF_6$ , is used. Among these,  $C_2H_2F_4$  serves as the primary medium for ionization.

#### 4.1.2 Streamer Mode

As the applied voltage increases, the gain ( $G$ ) rises, and at a certain threshold, photons start contributing to avalanche development, causing avalanches to spread. When the total charge in the avalanche approaches the point where space charge effects become significant, a plasma channel forms between electrodes, leading to spark formation and discharge of a local area due to bulk resistivity. This phenomenon, known as the Raether limit [39], occurs at pressures close to or higher than 1 atm and depends on the RPC's design, gas mixture, and pressure. In streamer mode, where charge generation is larger (about 50 pC to a few nC), subsequent amplification is unnecessary. However, this mode has a longer dead time, restricting operation to low count rate conditions. A gas mixture of argon and  $C_2H_2F_4$ , with a small amount of  $i-C_4H_{10}$  as a quencher, is used to operate in streamer mode.

## 4.2 Scattering angle distribution for an Iron block of size $100 \times 100 \times 100 \text{ mm}^3$

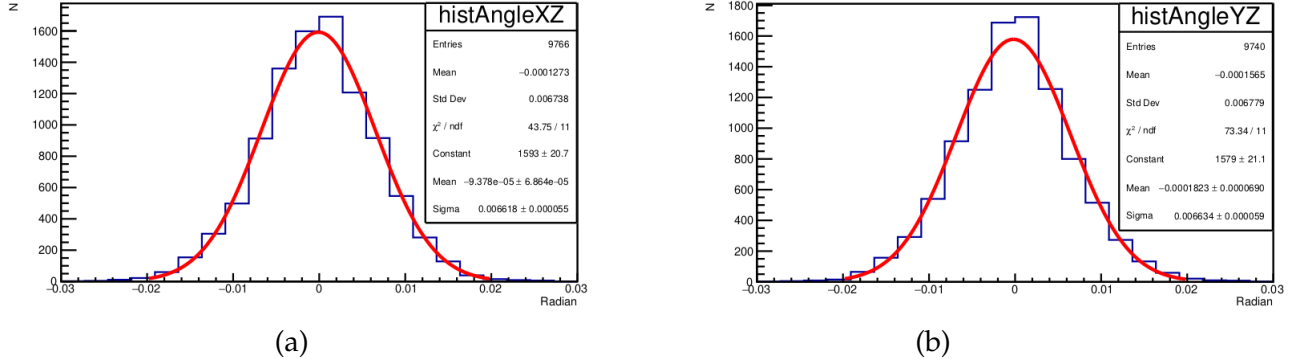


Figure 4.1: (a) Scattering angle distribution in XZ plane. (b) Scattering angle distribution in YZ plane.

## 4.3 Scattering angle distribution for Uranium block size $100 \times 100 \times 100 \text{ mm}^3$

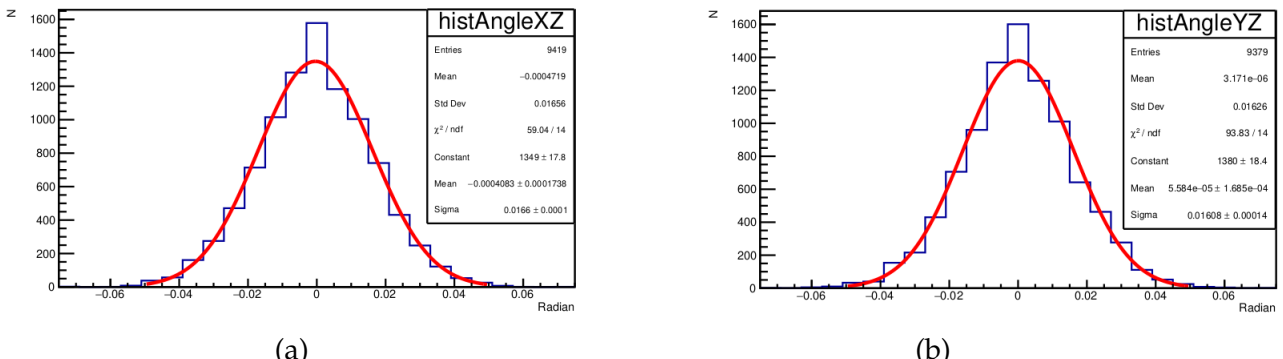


Figure 4.2: Uranium block of size  $100 \times 100 \times 100 \text{ mm}^3$  is used as target. (a) Scattering angle distribution in XZ plane. (b) Scattering angle distribution in YZ plane.

# References

- [1] J. C. Street and E. C. Stevenson. New evidence for the existence of a particle of mass intermediate between the proton and electron. *Phys. Rev.*, 52:1003–1004, Nov 1937.
- [2] Hideki Yukawa. On the interaction of elementary particles. i. *Proceedings of the Physico-Mathematical Society of Japan. 3rd Series*, 17:48–57, 1935.
- [3] Particle Data Group, P. A. Zyla, R. M. Barnett, J. Beringer, O. Dahl, D. A. Dwyer, D. E. Groom, C.-J. Lin, K. S. Lugovsky, E. Pianori, D. J. Robinson, C. G. Wohl, W.-M. Yao, et al. Review of Particle Physics. *Progress of Theoretical and Experimental Physics*, 2020(8):083C01, 08 2020.
- [4] DONALD E. GROOM, NIKOLAI V. MOKHOV, and SERGEI I. STRIGANOV. Muon stopping power and range tables 10 mev–100 tev. *Atomic Data and Nuclear Data Tables*, 78(2):183–356, 2001.
- [5] Luke C.L. Yuan and Chien-Shiung Wu. 1. fundamental principles and methods of particle detection. In *Nuclear Physics*, volume 5 of *Methods in Experimental Physics*, pages 1–288. Academic Press, 1961.
- [6] J.L. Autran, D. Munteanu, T. Saad Saoud, and S. Moindjie. Characterization of atmospheric muons at sea level using a cosmic ray telescope. *Nuclear Instruments and Methods in Physics Research Section A: Accelerators, Spectrometers, Detectors and Associated Equipment*, 903:77–84, 2018.

---

## REFERENCES

- [7] E. Rutherford. Lxxix. the scattering of alpha and beta particles by matter and the structure of the atom. *The London, Edinburgh, and Dublin Philosophical Magazine and Journal of Science*, 21(125):669–688, 1911.
- [8] Gerald R. Lynch and Orin I. Dahl. Approximations to multiple coulomb scattering. *Nuclear Instruments and Methods in Physics Research Section B: Beam Interactions with Materials and Atoms*, 58(1):6–10, 1991.
- [9] Particle Data Group. Review of particle physics: Cosmic rays. <https://pdg.lbl.gov/2022/reviews/rpp2022-rev-cosmic-rays.pdf>, 2022. Accessed on May 3, 2024.
- [10] Roger Blandford, Paul Simeon, and Yajie Yuan. Cosmic ray origins: An introduction. *Nuclear Physics B - Proceedings Supplements*, 256-257:9–22, 2014. Cosmic Ray Origin – Beyond the Standard Models.
- [11] W-M Yao et Al. Review of particle physics. *J. Phys. G Nucl. Part. Phys.*, 33(1):1–1232, July 2006.
- [12] Jeremy I. Pfeffer. *Modern Physics*. Imperial College Press, 2005.
- [13] EP George. Cosmic rays measure overburden of tunnel. *Commonwealth Engineer*, 43:455–457, 1955.
- [14] Luis W. Alvarez, Jared A. Anderson, F. El Bedwei, James Burkhard, Ahmed Fakhry, Adib Girgis, Amr Goneid, Fikhry Hassan, Dennis Iverson, Gerald Lynch, Zenab Miligy, Ali Hilmy Moussa, Mohammed Sharkawi, and Lauren Yazolino. Search for hidden chambers in the pyramids. *Science*, 167(3919):832–839, 1970.

- [15] Lorenzo Bonechi, Raffaello D'Alessandro, and Andrea Giammanco. Atmospheric muons as an imaging tool. *Reviews in Physics*, 5:100038, 2020.
- [16] Ralf Kaiser. Muography: overview and future directions. *Philosophical Transactions of the Royal Society A: Mathematical, Physical and Engineering Sciences*, 377(2137):20180049, 2019.
- [17] D Pagano, G Bonomi, A Donzella, A Zenoni, G Zumerle, and N Zurlo. Eco-Mug: An efficient COsmic MUon generator for cosmic-ray muon applications. *Nucl. Instrum. Methods Phys. Res. A*, 1014(165732):165732, October 2021.
- [18] S. Agostinelli and et. al. Geant4—a simulation toolkit. *Nuclear Instruments and Methods in Physics Research Section A: Accelerators, Spectrometers, Detectors and Associated Equipment*, 506(3):250–303, 2003.
- [19] Lorenzo Bonechi, Massimo Bongi, Davide Fedele, M. Grandi, Sergio Bruno Ricciarini, and E. Vannuccini. Development of the adamo detector: test with cosmic rays at different zenith angles. In *Development of the ADAMO detector: test with cosmic rays at different zenith angles*, 2005.
- [20] CMS Collaboration. Measurement of the charge ratio of atmospheric muons with the cms detector. *Physics Letters B*, 692(2):83–104, 2010.
- [21] Aatos Heikkinen, Nikita Stepanov, and J. P. Wellisch. Bertini intra-nuclear cascade implementation in geant4, 2003.
- [22] V. Uzhinsky. Tuning of the geant4 fritiof (ftf) model using na61/shine experimental data, 2011.
- [23] National Institute of Standards and Technology. Security requirements for cryptographic modules. Technical Report Federal Information Processing

- Standards Publications (FIPS PUBS) 140-2, Change Notice 2 December 03, 2002, U.S. Department of Commerce, Washington, D.C., 2001.
- [24] Rene Brun, Fons Rademakers, Philippe Canal, Axel Naumann, Olivier Couet, Lorenzo Moneta, Vassil Vassilev, Sergey Linev, Danilo Piparo, Gerardo GANIS, Bertrand Bellenot, Enrico Guiraud, Guilherme Amadio, wverkerke, Pere Mato, TimurP, Matevž Tadel, wlav, Enric Tejedor, Jakob Blomer, Andrei Gheata, Stephan Hageboeck, Stefan Roiser, marsupial, Stefan Wunsch, Ok-sana Shadura, Anirudha Bose, CristinaCristescu, Xavier Valls, and Raphael Isemann. root-project/root: v6.18/02, June 2020.
- [25] Sophie Wuyckens. Development of a compact telescope for cosmic muon flux and density measurements. Master's thesis, Centre for Cosmology, Particle Physics and Phenomenology, Université Catholique de Louvain, Belgium., 2022.
- [26] O. Adriani P. Achard and et al. Measurement of the atmospheric muon spectrum from 20 to 3000 gev. *Physics Letters B*, 598(1):15–32, 2004.
- [27] C Thomay, J J Velthuis, P Baesso, D Cussans, P A W Morris, C Steer, J Burns, S Quillin, and M Stapleton. A binned clustering algorithm to detect high-z material using cosmic muons. *Journal of Instrumentation*, 8(10):P10013, oct 2013.
- [28] Zhengzhi Liu. Methodologies for imaging a used nuclear fuel dry storage cask with cosmic ray muon computed tomography. *arXiv*, 2018.
- [29] The Southern States Energy Board (SSEB). Dry cask storage of nuclear spent fuel. Online.

- [30] Jin Ye, Cheng Jianping, Qian Yue, Li Yuanjing, Li Jin, and Wang Yi. Study on the position resolution of resistive plate chamber. *Nuclear Instruments and Methods in Physics Research Section A: Accelerators, Spectrometers, Detectors and Associated Equipment*, 591(2):411–416, 2008.
- [31] R. Santonico and R. Cardarelli. Development of resistive plate counters. *Nuclear Instruments and Methods in Physics Research*, 187(2):377–380, 1981.
- [32] Abhik Jash. *Studies on the physics of Resistive Plate Chambers in relation to the INO experiment*. PhD thesis, Calcutta, VECC, 2018.
- [33] Satyanarayana Bheesette. *Design and Characterisation Studies of Resistive Plate Chambers*. PhD thesis, Indian Inst. Tech., Mumbai, 2009.
- [34] Christian Lippmann and Werner Riegler. Detailed rpc avalanche simulations. *Nuclear Instruments and Methods in Physics Research Section A: Accelerators, Spectrometers, Detectors and Associated Equipment*, 533(1):11–15, 2004. Proceedings of the Seventh International Workshop on Resistive Plate Chambers and Related Detectors.
- [35] S. Narita, Y. Hoshi, K. Neichi, and A. Yamaguchi. Induced charge profile in a glass rpc operated in avalanche mode. *IEEE Transactions on Nuclear Science*, 60(6):4656–4659, 2013.
- [36] S. Narita, M. Shoji, Y. Hoshi, D. Miura, Y. Kikuchi, K. Neichi, and A. Yamaguchi. Measurements of induced charge profile in rpc with submilli-strips. *IEEE Transactions on Nuclear Science*, 57(4):2210–2214, 2010.
- [37] Antonello Pellecchia. The upgrade of the cms muon system for the high luminosity lhc, 2023.

---

REFERENCES

- [38] Ahmad Moshaii and Katayoun Doroud. Study the effect of humidity on the rpc performance. *Nuclear Instruments and Methods in Physics Research Section A: Accelerators, Spectrometers, Detectors and Associated Equipment*, 602(3):727–730, 2009. Proceedings of the 9th International Workshop on Resistive Plate Chambers and Related Detectors.
- [39] H. Raether. *Electron Avalanches and Breakdown in Gases*. Butterworths advanced physics series. Butterworths, 1964.